

Accepted Manuscript

Petrogenesis and origin of the Upper Jurassic-Lower Cretaceous magmatism in Central High Atlas (Morocco): Major, trace element and isotopic (Sr-Nd) constraints

Abderrahim Essaifi, Rachid Zayane



PII: S1464-343X(17)30381-3

DOI: [10.1016/j.jafrearsci.2017.10.002](https://doi.org/10.1016/j.jafrearsci.2017.10.002)

Reference: AES 3017

To appear in: *Journal of African Earth Sciences*

Received Date: 7 March 2017

Revised Date: 10 September 2017

Accepted Date: 4 October 2017

Please cite this article as: Essaifi, A., Zayane, R., Petrogenesis and origin of the Upper Jurassic-Lower Cretaceous magmatism in Central High Atlas (Morocco): Major, trace element and isotopic (Sr-Nd) constraints, *Journal of African Earth Sciences* (2017), doi: 10.1016/j.jafrearsci.2017.10.002.

This is a PDF file of an unedited manuscript that has been accepted for publication. As a service to our customers we are providing this early version of the manuscript. The manuscript will undergo copyediting, typesetting, and review of the resulting proof before it is published in its final form. Please note that during the production process errors may be discovered which could affect the content, and all legal disclaimers that apply to the journal pertain.

**Petrogenesis and origin of the Upper Jurassic-Lower Cretaceous
magmatism in Central High Atlas (Morocco): Major, trace
element and isotopic (Sr-Nd) constraints.**

ABDERRAHIM ESSAIFI*, RACHID ZAYANE

Geology Department, Cadi Ayyad University, B.P. 2390, Marrakech 40000, Morocco

Short title: High Atlas Upper Jurassic-Lower Cretaceous magmatism

* Corresponding author, essaifi@uca.ma

Tel +212 5 24 43 46 49 (work) +212 5 24 49 05 61 (home) Fax +212 5 24 43 74 11

Abstract

During an uplift phase, which lasted ca. 40 Ma, from the Late Jurassic (165 Ma) to the Early Cretaceous (125 Ma), transitional to moderately alkaline magmatic series were emplaced in the Central High Atlas. The corresponding magmatic products include basaltic lava flows erupted within wide synclines and intrusive complexes composed of layered mafic intrusions and monzonitic to syenitic dykes emplaced along narrow anticlinal ridges. The igneous rock sequence within the intrusive complexes is composed of troctolites, olivine-gabbros, oxide-gabbros, monzonites and syenites. The chemical compositions of the various intrusive rocks can be accounted for by crystal accumulation, fractional crystallization and post-magmatic remobilization. The evolution from the troctolites to the syenites was mainly controlled by a fractional crystallization process marked by early fractionation of olivine, plagioclase and clinopyroxene, followed by separation of biotite, amphibole, apatite, and Ti-magnetite. Hydrothermal activity associated with emplacement of the intrusions within the Jurassic limestones modified the elemental and the Sr isotopic composition of the hydrothermally altered rocks. In particular the monzonitic to syenitic dykes underwent an alkali metasomatism marked by depletion in K and Rb and enrichment in Na and Sr. As a result, their Sr isotopic composition was shifted towards higher initial Sr isotopic ratios (0.7067-0.7075) with respect to the associated gabbros (0.7036-0.7046). On the contrary, the Nd isotopic compositions were preserved from isotope exchange with the limestones and vary in a similar range to those of the gabbros ($+1.6 < \epsilon_{\text{Nd}} < +4.1$). The isotopic and the trace element ratios of the uncontaminated samples were used to constrain the source characteristics of this magmatism. The Sr-Nd isotopic data and the incompatible element ratios (e.g. La/Nb, Zr/Nb, Th/U, Ce/Pb) are consistent with generation from an enriched upper mantle similar to an ocean island basalt source. Melting of the subcontinental metasomatized lithosphere is tentatively related to small-scale shallow mantle upwelling and asthenospheric uprise at the triple junction between the western High Atlas, the Middle Atlas and the eastern High Atlas domains during a period of relative tectonic quiescence.

Key words: Continental intraplate magmatism, Sr-Nd isotopes, Lithospheric mantle, High Atlas, Morocco

1. Introduction

Understanding magmas generation and its related geodynamics in continental settings is generally difficult because crustal contamination and fractional crystallization may mask the source characteristics. This is evidenced by the wide range of the major, trace element and isotopic signatures of the continental intraplate basalts, which vary from those of Ocean Island basalts to those of continental crust (e.g. Wilson, 1993; Ma et al., 2013). Therefore, tracing the sources of the intraplate continental magmatism requires unravelling the complex history induced by interaction of these magmas with the lithospheric mantle and the continental crust during their ascent, storage and final emplacement.

In the High and the Middle Atlas intracontinental fold belt of Morocco, a significant magmatic activity occurred from the Mesozoic to the Quaternary. In a first stage, widespread tholeiitic basaltic lavas, part of the Central Atlantic Magmatic Province, were emitted at the end of the Triassic (e.g., Marzoli et al., 1999, 2004; Youbi et al., 2003; Knight et al., 2004; Nomade et al., 2007; V  rati et al., 2007); they were contemporaneous with a syn-rift Upper Permian-Late Triassic extensional phase related to the opening of the Atlantic Ocean to the west and the Tethys Sea to the north (Manspeizer et al., 1978; Manspeizer, 1988; Medina, 1995; Ellouz et al., 2003; Z  hlke et al., 2004). Then a petrologically diverse, but geographically restricted transitional to alkaline magmatism was emplaced in the Central High Atlas during a post-rift Jurassic–Cretaceous phase (Bera  ouz and Bonin, 1993; Zayane et al., 2000; Lhachnmi et al., 2001; Armando, 1999; Bensalah et al., 2013). This magmatism included layered intrusions, lavas flows, doleritic/gabbroic dykes and sills. The intraplate magmatic activity continued intermittently, emplacing carbonatites, lamprophyres and related dykes during the Late Cretaceous to Early Tertiary (ca. 67-57 Ma) at Taourirt in the northeastern end of the Middle Atlas (Wagner et al., 2003) and during the Eocene (ca. 45-35 Ma) at Tamazert in the High Atlas (Bouabdli et al., 1988; Bernard-Griffiths et al., 1991; Bouabdellah et al., 2010). Finally, an intraplate alkaline volcanic event emplaced nephelinites, basanites and alkali basalts from the Neogene to the Quaternary (16-0.6 Ma) along a Moroccan Hot Line extending from the Canary Islands to the Mediterranean (Maury et al., 2000; Teixell et al., 2005; Missenard et al., 2006; Duggen et al., 2009; El Azzouzi et al., 2010; Fullea et al., 2010; Missenard and Cadoux, 2012; Bosch et al., 2014).

The intrusive and extrusive transitional to alkaline magmatic activity of the Central High Atlas (CHA) spanned between ca. 165 and 125 Ma, possibly with two spikes, i.e. Late Jurassic and Early Cretaceous, and was coeval with a red bed sedimentation (Souhel, 1996;

Haddoumi et al., 2010; Charrière et al., 2011). The extrusive products are basaltic lava flows that outcrop in large synclines where they are intercalated within the red bed strata (Haddoumi et al., 2010; Frizon de Lamotte et al., 2008; Bensalah et al., 2013). The intrusive products are mafic and felsic intrusions that occupy NE-SW trending anticlinal ridges, and their emplacement was contemporaneous with a moderate synschistous deformation (Laville and Piqué, 1992) and halokinetic diapirism (Saura et al., 2013; Michard et al., 2011; Torres-Lopez et al., 2016).

Generation of such magmas in the Central High Atlas was attributed to (i) a Middle Jurassic transpressional tectonic phase indicating that the Atlas Mountains experienced a significant uplift and orogenesis during the Mesozoic (Laville and Piqué, 1992), (ii) a mantle plume or a mantle doming without significant crustal extension (Frizon de Lamotte et al., 2009; Michard et al., 2013), and (iii) a prolonged far-field extension of the Triassic continental rifting (Bensalah et al., 2013). In this paper we combine petrographic, major, trace element and Sr-Nd isotopic data on the CHA intrusive magmatism in order to constrain the petrogenetic processes, to explore the evolution and the source characteristics, and to discuss the tectonic models of the Central High Atlas during Late Jurassic-Early Cretaceous times.

2. Geological setting and geology of the Jurassic High Atlas magmatism

2.1. Geological setting

The Central High Atlas is part of the Cenozoic intracontinental belt that forms the Atlas Mountains extending from Morocco to Tunisia. This 40 to 100 km wide and 700 km long chain trends WSW-ENE (Fig. 1A). Its tectonic evolution and stratigraphy can be summarized as follows:

During Triassic times a rifting phase contemporaneous with the opening of the central Atlantic led to the individualization of the first subsiding basins in the High Atlas (Dewey et al., 1973; Lorenz, 1988). These basins were filled by more than 1 km of reddish continental sediments comprising sandstone, siltstone and evaporite-bearing shales (Mattis, 1977). These deposits were overlain by Upper Triassic to Lower Liassic tholeiitic basalts (Bertrand et al., 1982; Fiechtner et al., 1992; Beraâouz et al., 1994; Marzoli et al., 1999; Youbi et al., 2003; Verati et al., 2007). These basalts have isotopic ages ranging from 196 to 201 Ma (Sebai et al., 1991; Marzoli et al., 2004; Knight et al., 2004; Verati et al., 2007; Nomade et al., 2007; Blackburn et al., 2013; Davies et al., 2017).

During Jurassic times subsidence became important and led to deposition of up to 8 km of marine sediments (Studer, 1980). Liassic to Middle Jurassic sedimentation was essentially carbonaceous with intercalation of marls. Marine influence culminated during the Pliensbachian and the Bajocian; carbonaceous series were deposited essentially during the Sinemurian-Domerian and the Bajocian while marl series characterize the Toarcian and the Aalenian (Jacobshagen et al., 1988). After the Bajocian, a regional uplift occurred (Saddiqi et al., 2009) and sedimentation environments changed from marine to continental. Red strata essentially composed of sandstone were deposited from the Bathonian to the Barremian (Jenny et al., 1981; Souhel and Canérot, 1989; Charrière et al., 2005; Haddoumi et al., 2010). Basaltic flows occur in two sequences (Brechtbühler et al., 1988; Laville and Piqué, 1992; Haddoumi et al., 2010; Bensalah et al., 2013) intercalated within the Bathonian-Callovian and the Barremian, respectively.

During the Cretaceous and the Tertiary, continuous Aptian to Eocene marine sedimentary series were deposited in the northern and the southern borders of the Central High Atlas (Fraissinet et al., 1988; Görler et al., 1988). The Aptian formations are sandstones with intercalations of dolomites and gypsum-bearing marls. They are overlain by Cenomanian-Turonian carbonates (Ferrandini et al., 1985). In the central part of the High Atlas, the Aptian to Eocene marine sedimentary series are however absent or reduced to some Cenomanian to Aptian calcareous shreds and Cenozoic continental sandstones (Ibouh, 2004). Finally, both synsedimentary unconformities and elements of the Oligo-miocene conglomerates indicate that uplift of the High Atlas began during the Miocene or the Oligocene time (Görler et al., 1988; Michard et al., 2011).

Presently the Central High Atlas displays folds and NE-SW to ENE WSW striking thrusts (Fig. 1A). Wide and open Middle Jurassic-cored synclines are separated by narrow Lower Jurassic-cored anticlines where the magmatic intrusions outcrop (Fig. 1B).

2.2. Geology of the Jurassic High Atlas magmatism

During Jurassic times, the Central High Atlas area was composed of numerous elliptical to subcircular small-size basins <30 km wide, controlled by sinistral strike-slip faults, and separated by synsedimentary diapiric anticlinal ridges striking in three principal directions: N45°, N70° and N120° (Laville and Piqué, 1992; Saura et al., 2013) (Figs. 1B, 2). The NE anticline structures are generally composed of Triassic red shales, evaporitic series and flow

basalts, with meter- to hectometre-scale slivers of Liassic to Dogger carbonaceous and marl-carbonaceous sedimentary formations, and their axes are occupied by magmatic intrusions. The whole anticline structure is unconformably overlaid by Palaeocene non-marine red beds (Charrière et al., 2009), whose peculiar geometry of folded red bed synclines (Fig. 2) has been related to Mesozoic halokinesis and superimposed Cenozoic shortening (Michard et al., 2011). The basins are filled by 3-4 km thick Lower to Middle Jurassic deposits comprising halokinetic sequences (Saura et al., 2013).

The magmatic ridges form elongated layered intrusions generally delimited by tectonic contacts with the country rocks (Figs. 1B, 2). Non-faulted boundaries corresponding to chilled margins are locally present and marked by microgabbros at the contact between the intrusions and the host rocks. The tectonic contacts are mostly vertical faults marked by breccia composed of very poorly sorted polygenic clasts of gabbros and carbonates (1-50 cm in diameter) enclosed within a loose and fine-grained pelitic or carbonaceous matrix. Contact metamorphic aureoles are almost absent around the intrusions, which are pervasively faulted. The faults fragmented each intrusion into several blocks (Fig. 3), partially hiding primary relationships. In agreement with Armando (1999), we interpret the numerous and widespread Upper Triassic to Lower Liassic carbonates and pelites with subordinate altered basalts that lie within the intrusions as roof pendants formed during tectonic extrusion of the magmatic rocks.

The layered intrusions are composed of medium- to coarse-grained mafic rocks and granular to fine-grained intermediate-felsic rocks of monzonitic to syenitic composition (Fig. 4a-c). The mafic rocks show a cm-scale layering (Fig. 4d) and consist of ortho-cumulates or poikilitic ortho-cumulates (Fig. 4e) with olivine (Fo_{55-81}), plagioclase (An_{60-70}) and clinopyroxene (augite, $\text{Wo}_{40-45}\text{En}_{40-50}\text{Fs}_{8-15}$) as cumulus phases (55-80 vol.%), ilmenite \pm magnetite rimmed by biotite (titaniferous phlogopite, $X_{\text{Mg}} = 0.75$) \pm hornblende (kaersutite), as intercumulus phases (45-20%). The latter could also include apatite and sulphide minerals such as pyrite, chalcopyrite, pyrrhotite and pentlandite (Chèvremont, 1975). Olivine is typically equant with subrounded edges, ranging in size from 4 mm to < 1mm, generally enclosed by clinopyroxene or plagioclase. In a few cases olivine presents triple-point junctions and inclusions of plagioclase and Cr-spinel grains. Plagioclase has euhedral to anhedral shapes and ranges in size from 5 mm to <1 mm. Most of the grains are elongate and show a preferential orientation. Clinopyroxene is generally poikilitic and includes both olivine and plagioclase grains.

There is an upward decrease in the olivine content marked by an evolution from a lower series made up by troctolites to an upper series made up by olivine-gabbros and oxide-gabbros. Troctolites are characterized by abundant olivine (40-50%) and plagioclase (35-40%) relatively to clinopyroxene (<10%). Anorthosite and leucogabbro layers (plagioclase >65%) were also described in some intrusions (Armando, 1999; Saidi, 1992). Olivine-gabbros are composed of abundant plagioclase (45-55%) and clinopyroxene (20-25%) relatively to olivine (8-26%). Oxide-gabbros are olivine-free and contain 4-6% Fe-Ti oxides in addition to plagioclase and clinopyroxene; The Fe-Ti oxides occur as disseminated ilmenite and titanomagnetite grains rimmed by biotite and/or brown amphibole. Oxide-rich gabbros with up to 10% magnetite occur in the nearby Jbel Hayim (Anefgou) intrusion (Armando, 1999).

A secondary mineral association including actinolite/tremolite, chlorite, scapolite, prehnite, epidote, titanite, albite and calcite, is heterogeneously distributed within the mafic rocks. In spite of secondary transformation, magmatic textures are preserved and allow identification of the protoliths. The gabbroic rocks highly affected by alteration processes present either a laminated texture (flow texture) marked by the preferred orientation of liquidus phases (plagioclase), or microgranular, granular and pegmatoidal textures, sometimes with cm-scale amphiboles. They contain up to 45% actinolite that is present as poekilitic, fibrous or acicular crystals including relicts of augite ($\text{Wo}_{41-48}\text{En}_{38-42}\text{Fs}_{9-17}$) and phlogopite ($X_{\text{Fe}} = 0.4-0.9$). Plagioclase is rimmed by albite and prismatic apatite and titanite are also present. The accessory minerals include magnetite, ilmenite and/or pyrite and chalcopyrite (Fig. 4f). The gabbros with a widespread secondary mineral association (>40%) are here classified as hydrothermally altered gabbros.

Fine-grained mafic rocks are microgabbros forming metric dykes that crosscut both the intrusions and the country rocks and chilled margins at the contact between the coarse-grained mafic rocks and the sedimentary formations. Their texture varies from doleritic to porphyritic, and their primary mineralogy is similar to that of the coarse-grained mafic rocks, being composed of olivine, plagioclase, clinopyroxene, brown amphibole and Ti-oxides as the primary minerals. Some very fine-grained microgabbros found in chilled margins are olivine- and pyroxene-free, and mainly characterized by brown-amphibole and plagioclase phenocrysts within a matrix composed of idiomorphic small plagioclase laths, green amphibole and Ti-oxide grains. A low-temperature secondary mineral association composed of prehnite, actinolite, chlorite, epidote, calcite and sphene is well developed in the microgabbros.

The intermediate to felsic rocks are monzonites and syenites that are structurally above the mafic rocks or form up to 1 km-thick subvertical intrusive megadykes (Fig. 4b). Numerous minor syenitic dykes, up to 3 m-thick, cut across the troctolites and the gabbros (Fig. 4c). The monzonites are rare. They are spatially associated to the syenitic rocks and form the outer parts of the felsic megadykes in the Jbel Hayim intrusion. The monzonites present an isogranular texture and rarely an agpaitic texture. They contain up to 30% Fe-rich biotite and acicular brown amphibole (Fe-richterite; Armando, 1999). Altered tabular plagioclase laths are surrounded by perthitic alkali feldspar while quartz-feldspar granophyric associations are locally present. Acicular Ti-oxides are surrounded by amphibole. Sphene and apatite are abundant. Primary amphibole is commonly altered to actinolite. Epidote and calcite are the most common accessory minerals.

The syenitic rocks are fine (millimetre)-grained at the outer parts of the dykes and coarse (centimetre)-grained in the inner parts of the dykes. They general present an agpaitic texture and their mineralogy is dominated by idiomorphic K-feldspar (30-65% of orthoclase and microcline), and contain less than 15% of albitic plagioclase (An_{7-10}), up to 10% interstitial quartz and less than 5% biotite and amphibole (hastingsitic hornblende, Armando, 1999). The modal compositions of the felsic rocks correspond to quartz-syenites and syenites. The most common accessory minerals are titanite, allanite, apatite and zircon. Perthite can be abundant while quartz-feldspar granophyric associations can be present (Fig. 4g, h). Such granophyric intergrowths of quartz and alkali feldspar suggest subsolidus replacement of feldspar by quartz, although late magmatic eutectic crystallization cannot be ruled out. The secondary mineral association includes epidote, calcite, muscovite, albite, actinolite/tremolite, chlorite, prehnite and titanite.

Crystallization temperatures for magmatic amphiboles calculated with the Ti-in-amphibole thermometer of Otten (1984) yields 950-1043 °C for kaersutite crystallization in the mafic cumulates. Emplacement of the intrusions into still wet and reactive sediments resulted in up to 2 km wide hydrothermal alteration aureoles around the intrusions (Laville et al., 1994). Locally, the occurrence of a contact metamorphic aureole, marked by recrystallization of Bajocian and Bathonian carbonates, with development of titanite, tourmaline, anatase, Mg-chlorite and garnet (grossular-andradite) (Armando, 1999, Lhachmi et al., 2002), allowed estimation of metamorphic temperatures up to 500°C (Lhachmi, 1992). In the Triassic basaltic host rocks the hydrothermal alteration is marked by development of fractures sealed by calcite, epidote, chlorite, quartz, prehnite and/or analcite. In the Triassic to Bathonian

sedimentary host rocks the hydrothermal veins were sealed by scapolite, talc and clay minerals, smectite, interstratified illite/smectite and chlorite/smectite minerals. In the magmatic intrusive rocks superposed secondary parageneses developed during hydrothermal alteration (Laville et al., 1994; Zayane et al., 2001). A paragenesis composed of Cl-rich pargasitic hornblende, marialite type scapolite and talc was formed at amphibolite facies temperatures ($T \approx 500-650^\circ\text{C}$). Then at greenschist facies temperatures ($T \approx 450-350^\circ\text{C}$) a paragenesis composed of actinolite/tremolite, chlorite, albite, sphene, serpentine and calcite was developed. It was followed by a paragenesis composed of prehnite, actinote, chlorite, epidote, quartz and calcite, which formed at temperatures between 350 and 300°C (prehnite-actinote facies). Finally laumontite and analcite appeared at the lowest temperatures recorded in the intrusions ($T \leq 200^\circ\text{C}$), which represent temperatures of the thermal re-equilibration of the intrusions with the sedimentary country rocks. Moreover, in the Central High Atlas ore-bearing structures are closely related to the magmatic intrusions, which host a Cu–Ni mineralization (Chèvremont, 1975) and a disseminated Zn–Pb mineralization of hydrothermal origin (Caña, 1968; Choulet et al., 2013). A genetic link is also suggested between the magmatic intrusions and Zn–Pb ore bodies located within the calcareous host rocks (Mouguina, 2004).

3. Sampling and analytical methods

Samples weighing up to 5 kg and representing the major rock types exposed in the Tassent, Tirrhist and Tasraft intrusions were collected, and representative whole rock geochemical data are presented in Table 1. Sample locations and complete analytical data are available in Zayane (1992; 2001). The samples were analyzed for both major- and trace-elements at the Centre de Géochimie de la Surface at CNRS Strasbourg (France). The overall chemical compositions (including REEs) were determined by an ARL type 35000C Inductively Coupled Plasma-Atomic Emission Spectrometry (ICP-AES) and Corning Flam emission Spectrometer (Corning Medical type EEL 450) for Na and K (Samuel et al., 1985).

The samples for the analysis were powdered in a carbon steel mill, dried at 110°C for 12 hours, and then calcined at 1000°C for 3 hours. The difference between dried and calcined samples allowed to define Loss-on-ignition (L.O.I). 100 mg of the calcined samples were mixed with 750 mg of lithium tetraborate in a glassy graphite and fused at 1000°C under inert Ar atmosphere. The molten melt was then dissolved into solution of dilute nitric acid

(HNO₃) and glycerine (Samuel et al., 1985). The accuracy of the analyses was determined by comparison with 4 international standards from CRPG Nancy (AN-G, BE-N, GS-N and VS-N). The reference values used are those of Govindaradju (1995). The precision of the analyses is $\pm 2\%$ for the major elements and $\pm 5\%$ for the trace elements.

Some samples (labelled with asterix on Table 1) were analysed at Saint Mary's University Halifax. Major and trace elements (Sr, Ba, V, Ni, Cr, Zn, Cu, Zr, Y, Nb, Th, Ga, Rb) have been analysed by X-ray fluorescence. The precision and accuracy of the data are generally better than $\pm 10\%$ for the major elements and smaller than 5% for the trace element analyses. Some samples were run at both laboratories and yielded similar results, indicating that the major and trace element data from the two laboratories are in good agreement.

For Sr–Nd isotopic studies eight samples were selected from the Tirrhist intrusion in order to cover the range of lithological variation within this intrusion (Fig. 3). The selected samples include three oxide-gabbros, one hydrothermally altered gabbro, one monzonite and three syenites. Whole rock Sr–Nd isotopic analyses were carried out at the Centre de Recherches Pétrographiques et Géochimiques (CRPG, Vandoeuvre-les-Nancy), using a Finnigan MAT 262 multicollector mass spectrometer. The chemical separation procedures are those described by Alibert et al. (1983) for Rb–Sr, and Richard et al. (1976) for Sm–Nd. During the course of this study, the NBS 987 Sr standard yielded $^{87}\text{Sr}/^{86}\text{Sr}$ values of 0.710190 ± 10 , and the La Jolla (Nd) standard yielded $^{143}\text{Nd}/^{144}\text{Nd}$ values of 0.511845 ± 12 . All measured $^{87}\text{Sr}/^{86}\text{Sr}$ were normalized to $^{86}\text{Sr}/^{88}\text{Sr} = 0.1194$ and measured relative to NBS 987 Sr Standard = 0.71025. The error of $^{87}\text{Sr}/^{86}\text{Sr}$, including the statistical error obtained during the mass spectrometer run and other error sources such as instrumental reproducibility, is estimated to be ± 0.0003 . Nd isotopic ratios were normalized to $^{146}\text{Nd}/^{144}\text{Nd} = 0.7219$. The results are presented in Table 2. The samples of the Eocene Tamazert alkaline rocks, previously analysed for Sr and Nd isotopes by Bernard-Griffiths et al. (1991) and Bouabdellah et al. (2010), are also plotted for comparison.

4. Results

The mafic rocks are mostly layered troctolites and gabbros formed by cumulate processes while some rocks found in dykes and chilled margins more likely represent magmatic compositions. High MgO (c. 12–19 wt %), Fe₂O₃* (total Fe as Fe₂O₃ c. 12.6–15.5 wt %), Cr, Co and Ni contents due to olivine accumulation characterize the troctolites while higher CaO

(c. 8-11 wt %), Al_2O_3 (c. 14.3-18.2 wt %) and Sr (385-813 ppm) contents reflect plagioclase accumulation in the olivine-gabbros and oxide-gabbros (Table 1). There is a regular decrease in the Mg no. ($\text{Mg}^{2+}/\text{Mg}^{2+}+\text{Fe}^{2+}$, assuming $\text{Fe}_2\text{O}_3/\text{FeO}=0.18$) from troctolites ($0.67\leq\text{Mg no}\leq 0.72$) to olivine-gabbros ($0.57\leq\text{Mg no}\leq 0.63$) and oxide-gabbros ($0.40\leq\text{Mg no}\leq 0.46$). In the element binary plots against MgO (Fig. 5), the decrease in MgO from troctolites to oxide-gabbros is accompanied by an increase in TiO_2 , CaO, Sr and V, and a decrease in Cr and Ni. Evolution from troctolites to olivine-gabbros is characterized by an increase in SiO_2 , Al_2O_3 , CaO and Na_2O , and a decrease in Fe_2O_3^* while the evolution from olivine-gabbros to oxide-gabbros is characterized by an increase in Fe_2O_3^* and a decrease in SiO_2 while Al_2O_3 is roughly constant. Cu parallels Fe_2O_3^* indicating precipitation of Cu-bearing sulphide minerals in oxide-gabbros. Such trends between oxide-rich gabbros, olivine gabbros and troctolites are similar to those described in the nearby Jbel Hayim massif by Armando (1999) and seem to characterize the CHA intrusives.

The loss on ignition (LOI) in the hydrothermally altered gabbros is higher than in troctolites, olivine-gabbros and oxide-gabbros and reach 4.58 wt%. Their bulk compositions overlap with those of olivine-gabbros and oxide-gabbros, except for those elements that are highly mobile in aqueous fluids. For instance their CaO and Sr contents are lower than those of the olivine-gabbros and oxide-gabbros and reach 2 wt% and 35 ppm respectively in the sample with the highest LOI (Table 1). In the element binary plots against MgO (Fig. 5), the hydrothermally altered gabbros data points scatter between olivine-gabbros, oxide-gabbros and microgabbros. The microgabbros were sampled in chilled margins around the troctolites of the Tasraft intrusion. They show relatively high LOI percentages (c. 3 wt%) and large variations in elements that are highly mobile in aqueous fluids, i.e. K_2O , Na_2O , CaO, Ba and Sr. The other elements have almost similar contents in the two chilled margins but these have higher TiO_2 , V, Al_2O_3 , SiO_2 and Zr, and lower MgO, Fe_2O_3^* , Ni and Cr contents than the adjacent troctolites.

The monzonitic samples have similar SiO_2 contents (56.5-57.1 wt %) but different LOI percentages (0.3-2.96 wt %). Their contents in MgO, Zr, Y, Co, Nb and Yb, are similar but their contents in CaO, Fe_2O_3^* and Sr are variable. Comparatively to the most differentiated gabbros, the monzonites are depleted in MgO, CaO, TiO_2 , V, Co, Ni, Cr and Ni, and enriched in Na_2O , Zr, Y, and Yb. Comparatively to the monzonites of the Jbel Hayim intrusion (Armando, 1999), the monzonitic samples of Tasraft and Tirrhist intrusions have low K_2O and Rb contents. The syenites are characterized by SiO_2 contents exceeding 60 wt% and MgO

contents generally lower than 1 wt %. Comparatively to the monzonites, the syenites have generally lower TiO_2 , P_2O_5 and CaO contents and higher Yb contents. Al_2O_3 (c. 14.4-18.4 wt %), Fe_2O_3^* (2-11 wt%), Na_2O (c. 6.2-9.7 wt%), K_2O (c. 0.3-4.6 wt%), Sr (c. 43-762 ppm), Ba (c. 62.9-675 ppm), Zr (c. 215-78 ppm) and Rb (c. 9-40 ppm) show large variations than in the monzonites.

The Harker diagrams of figure 5 show a regular decrease in MgO from troctolites to syenites accompanied by an increase in SiO_2 with a noticeable compositional gap between oxide-gabbros and monzonites. TiO_2 and CaO increase from troctolites to oxide-gabbros then decrease in monzonites and syenites while Al_2O_3 increases from troctolites to olivine-gabbros and is roughly constant in monzonites and syenites. Fe_2O_3^* and MnO decrease from troctolites to olivine-gabbros then increase significantly in oxide-gabbros and show a large variation in monzonites and syenites. $\text{Na}_2\text{O}+\text{K}_2\text{O}$ show an increase from troctolites to monzonites and syenites. From troctolites to syenites there is an increase in Nb, Y, Zr and Yb while Cr, Co and Ni show a decrease (Fig. 5B). V and Sr parallel TiO_2 and CaO by showing an increase from troctolites to oxide-gabbros followed by a decrease in monzonites and syenites. Ba and Rb show a general increase with decreasing MgO but large variations occur in the syenites. Similarly CaO and Sr vary largely in the hydrothermally altered gabbros. Such large variations at relatively constant MgO contents point to postmagmatic remobilization.

On the total alkali-silica (TAS) diagram the samples plot in the alkaline field or along the boundary between the alkaline and the subalkaline fields (Fig. 6). Using the classifications scheme of Frost et al. (2001), most of the felsic rocks plot in the ferroan granites field while some samples are magnesian granites. In the $(\text{Na}_2\text{O}+\text{K}_2\text{O}-\text{CaO})$ vs. SiO_2 diagram most of the samples plot within the alkalic granitoids (Fig. 7). Thus most of the monzonites and syenites of the High Atlas intrusive rocks are classified as ferroan (A-type) metaluminous alkalic granitoids.

The REE increase from oxide-gabbros and hydrothermally altered gabbros ($\sum\text{REE}=44-65$ ppm) to monzonites and syenites ($\sum\text{REE}=122-230$ ppm). The gabbros and some monzonites show positive Eu anomalies probably due to plagioclase accumulation while the syenites show mostly negative Eu anomalies (Fig. 8). The REE patterns in the oxide gabbros are characterized by uniform and slightly enriched REE patterns with moderate LREE to HREE fractionation [$(\text{La}/\text{Yb})_N = 3.62-4.36$, $(\text{La}/\text{Sm})_N = 1.47-1.69$], where N stands for chondrite normalized values according to McDonough and Sun (1995)], slight to moderate positive Eu anomalies ($\text{Eu}/\text{Eu}^*=1.21-1.45$) and slightly fractionated HREE chondrite-normalized patterns

((Gd/Yb) N = 1.78–1.89). The REE pattern of the hydrothermally altered gabbro is slightly enriched in LREE and depleted in HREE relatively to the oxide-gabbro [(La/Yb) N = 5.87, (La/Sm) N = 1.93]. The two monzonitic samples are characterized by superposed REE patterns with a moderate LREE/HREE fractionation ((La/Yb) N = 4.69–6.28, (La/Sm) N = 1.97–2.38)), a positive Eu anomaly (Eu/Eu* = 2.01–1.13), and moderately sloping HREE chondrite-normalized patterns ((Gd/Yb) N = 1.64–1.80). The syenites are characterized by a moderate LREE to HREE fractionation ((La/Yb) N = 4.69–7.88, (La/Sm) N = 2.24–3.34)), highly negative to positive Eu anomalies (Eu/Eu* = 0.3–1.27) and flat to moderately sloping HREE chondrite-normalized patterns ((Gd/Yb) N = 1.20–1.66).

In the primitive mantle normalized multielement diagrams (Fig. 9), the oxide-gabbros are characterized by uniform and flat to slightly enriched patterns with positive Sr and Ti anomalies due respectively to plagioclase and ilmenite accumulation while the Nb (=16 Hf) anomaly is absent. The pattern of the hydrothermally altered gabbro is similar to those of oxide-gabbros except for enrichments in Rb and Ba that reflect mobilization during hydrothermal alteration. The REE contents of the oxide-gabbros and hydrothermally altered gabbros range from 12.4 to 40.6 ppm for Ce, from 0.2 to 0.7 ppm for U and from 2 to 7 ppm for Pb. The syenites have also flat to slightly enriched multielement patterns with most samples showing negative anomalies in Sr, Ti and P. The monzonites have patterns similar to those of the syenites, with negative anomalies in Ti and P and either positive or negative anomalies in Sr. No Nb anomaly is observed in both the monzonites and the syenites.

Sr-Nd isotopic data for eight samples including oxide-gabbros, hydrothermally altered gabbros, monzonites and syenites are given in Table 2 and shown as a plot of ϵ_{Nd} vs. initial Sr isotopic ratios calculated at 150 Ma (Fig. 10). This age is constrained from bisotratigraphic studies of the red beds hosting the CHA basalts (Haddoumi et al., 2010), from K-Ar ages of the basaltic lava flows (Westphal et al., 1979) and from Ar-Ar ages of the CHA intrusives (Armando, 1999), which allow to ascribe this magmatic activity to ca. 165–125 Ma (Michard et al., 2011). In particular $^{40}Ar/^{39}Ar$ ages obtained on biotite separates from troctolites and olivine-gabbros of the nearby Jebel Hayim massif are ranged in two distinct intervals: 151 ± 1 Ma to 147 ± 1 Ma (isochrones) and 151.3 ± 0.5 Ma to 145.0 ± 0.5 Ma (plateau ages). Despite geochemical differences, oxide-gabbros, hydrothermally altered gabbros, monzonites and syenites have similar initial ϵ_{Nd} values, ranging from +1.6 to +4.1. However, the monzonite and syenites initial Sr isotopic ratios (0.7067–0.7075) are higher than those of oxide-gabbros (0.7036–0.7046) while the hydrothermally altered gabbro has an intermediate initial Sr

isotopic value (0.7048). Thus the oxide-gabbros plot within the mantle array while the syenites and monzonite plot outside this field.

5. Discussion

5.1. Magmatic affinities

Since the alkali and alkali earth elements are generally mobilized during hydrothermal alteration (see below), the alkaline to subalkaline affinity indicated by the TAS diagram (Fig. 6) should be questioned. Based on immobile-discrimination diagrams such as Zr/Ti vs. Nb/Y of Winchester and Floyd (1977), the CHA mafic rocks plot along the boundary between the alkaline and the subalkaline fields. The clinopyroxene compositions also plot in both the alkaline and the subalkaline fields in the Ti versus Ca+Na diagram of Leterrier et al. (1982) pointing to a transitional rather than a purely alkaline affinity (Zayane, 1992). The TiO₂ and P₂O₅ contents of the CHA mafic rocks are lower than those of the intraplate alkaline mafic rocks and only some samples present normative nepheline. A transitional affinity is further supported by La/Yb ratios, which are lower than 10 in most of the CHA intrusives (Kay and Gast, 1973), and extrusives as well (Bensalah et al., 2013). With generally flat to slightly enriched patterns, the primitive mantle normalized multielement diagrams of the CHA intrusives are less enriched than those of typical intraplate alkaline series (Fig. 9); they are similar to those of continental tholeiites and transitional basalts (Dupuy and Dostal, 1984; Cook et al., 2005). In the Ti+Cr versus Ca diagram of Leterrier et al. (1982), the clinopyroxene compositions of both the CHA Late Jurassic-Early Cretaceous intrusives and extrusives plot in the field of non-orogenic basalts (Zayane, 1992; Bensalah et al., 2013). This anorogenic character of the studied rocks is also evidenced by the use of immobile-element discriminant diagrams based on whole rock compositions (Zayane, 1992; Bensalah et al., 2013). The high Zr/Y ratios, relatively high Ti/V ratios and TiO₂ contents, and lack of negative Nb anomalies of the CHA mafic rocks indicate that they are clearly distinct from arc basalts. Their Ce/Pb ratios are low (2.4-6.6 in the gabbroic rocks and 2-21 with a mean of 9.4 in the basalts) and similar to those of the transitional to quartz-tholeiitic lavas of the New Volcanic Province of Southeast Australia (Price et al., 1997; Cook et al., 2005). On the basis of the whole rock and mineral compositions we consider the Late Jurassic-Early Cretaceous CHA intrusives as belonging to a transitional to moderately alkaline intraplate series, similar to the basaltic magmatism intercalated within the Jurassic-Cretaceous red beds of the CHA

(Bensalah et al., 2013), and that both represent intrusive and extrusive igneous materials most likely emplaced during the same magmatic event.

5.2. Fractional crystallization

The common observation of magmatic layering and cumulate textures, as well as the variations observed in the major and trace element compositions of the CHA igneous rocks, suggest that their evolution was mainly controlled by in situ fractional crystallization. MgO shows a progressive decrease with differentiation whereas Ti, Ca, Al and P increase from the troctolites to the oxide-gabbros then decrease in the monzonites and syenites (Fig. 5). While the main trend from troctolites to syenites is an increase of SiO_2 and a decrease of Fe_2O_3^* , the oxide-gabbros are also characterized by a decrease in SiO_2 and an increase in Fe_2O_3^* indicating precipitation of Fe-Ti oxides. These variations are consistent with fractionation of olivine, plagioclase, and clinopyroxene, followed by amphibole, biotite, apatite and Ti-magnetite. Accumulation and fractionation of such minerals is respectively supported by the normalized trace elements patterns, which show positive anomalies in Eu, Sr and Ti in the gabbros and negative anomalies in Eu, Sr, Ti and P in the syenites (Fig. 10), suggesting that fractional crystallization was a prominent process in the evolution from the troctolites to the syenites. During this process precipitation of Fe-Ti oxides played a major role in the evolution from the mafic to the felsic rocks. The role of Fe-Ti oxide crystallization in the formation of A-type granitoids and the Daly gap has been recognized in other intrusive complexes including layered mafic intrusions and syenites (Shellnutt et al., 2009). The crystallization order (olivine, plagioclase and clinopyroxene), and the low Al contents of clinopyroxene and amphibole indicate crystallization at low pressure (Wass, 1979; Hollister et al., 1987), within magma chambers located at upper crustal levels (10-15 km depth), at the bottom of the Mesozoic cover (Zayane, 1992; Armando, 1999; Lhachmi et al., 2001). Vertical movements along pre-existing faults, probably favoured by halokinetic diapirism (Michard et al. 2011; Saura et al., 2013), resulted in the uprise of the still-cooling intrusions toward their present location, i.e. within the mid-Jurassic sequences.

The trace element and isotopic data indicate that both mafic and felsic rocks are cogenetic. Isotopically the monzonites and syenites have initial ϵ_{Nd} values (+1.6 to +4.1) similar to those of the gabbroic rocks (+2.0 to +3.7) indicating that they may have originated from similar parental magmas. The Th/U (2.1-3.5) and Hf/Ta (2.2-5.4) ratios of both gabbroic and syenitic rocks are similar and resemble those of ocean island basalts (Sun and McDonough,

1989; Weaver, 1991a). However, increases of incompatible elements (e.g. Th, Y) from the troctolites to the syenites are not strictly linear and a significant variation in the incompatible element ratios (e.g. Nb/Y, La/Nb, Zr/Nb, Ce/Zr) exists in the igneous rock sequence (Fig. 11), suggesting that not all the geochemical variations can be related to fractional crystallization, and that the contributions of other processes, i.e. crustal contamination and/or generation from different sources, are required.

5.3. Hydrothermal alteration, alkali metasomatism and crustal contamination

Sr-Nd isotopic data show that the CHA igneous rocks have similar ϵ_{Nd} values but highly variable initial Sr isotopic ratios, with the highest initial Sr isotopic ratios in the monzonitic and syenitic rocks (Fig. 10). Since the whole rock Sm-Nd system is more resistant to late-stage low-grade perturbations than the Rb-Sr system, this indicates that the scatter of whole-rock Rb-Sr data can simply be related to post-magmatic perturbations. Such perturbations are consistent with the scatter observed for K_2O , CaO, Na_2O , Rb and Ba in Harker diagrams, especially in the hydrothermally altered gabbros and the felsic rocks (Fig. 5). The lack of trends that could be explained by magmatic processes suggests that variation of these elements is a function of superposition of metasomatic and magmatic processes. In the monzonitic and syenitic rocks, K and Rb display a negative correlation with Na and an increase in CaO and Sr with decreasing Na_2O contents (not shown). Such relationships suggest an albitization process (Ragland, 1989; Drummond et al., 1986; Elburg et al., 2001) during which the syenites were enriched in Na, so that their Na_2O content reaches 10 wt %, and impoverished in K, so that their K_2O content reaches 0%. This alkali metasomatism was accompanied by enrichment of the syenites in radiogenic Sr, which shifted their initial Sr isotopic ratios to higher values compared to the cogenetic gabbros. Such a difference in the Sr isotopic composition between the gabbros and the syenites has also been described by Lutz et al. (1988) in the alkaline complex of Abu Khruq in Egypt. It is related to the fact that the gabbros have much higher Sr concentrations than the syenites, which made the Sr isotope composition of the gabbros less sensitive to hydrothermal alteration. This is most likely the reason why the shift in the initial Sr isotopic ratio of the hydrothermally altered gabbro ($Sr_i=0.7048$) is less important than in the monzonitic and syenitic rocks. The shift of the Sr isotopic compositions toward higher values while the Nd isotopic compositions were not affected was also described in the neighbouring lamprophyre dykes and carbonatites intruding the Jurassic limestones in the alkaline Tamazert complex of the Central High Atlas (Fig. 9).

These variations were related to fluid-driven interactions between the dykes and Sr-rich-Nd-poor Jurassic limestones (Bernard-Griffiths et al., 1991; Bouabdellah et al., 2010). The model mixing curve between the less contaminated gabbro and the Jurassic limestones indicates that addition of 55 to 75% of Sr from the host limestone can account for the Sr isotopic composition of the monzonite and syenite samples (Fig. 10). The widespread development of Na-rich scapolite among the hydrothermal products of the CHA intrusions (Zayane et al., 2001), and that of albite rims around feldspars (Fig. 4f, h), support contamination of the syenites by selective Sr isotopic exchange in the presence of a fluid phase during late stage crystallization of the matrix.

5.4. Source characteristics

The field evidences for close spatial and temporal association and the conclusions of the petrogenetic study indicating an evolution mainly controlled by a fractional crystallization process suggest that the various rock types of the CHA are roughly cogenetic and likely derived from the same kind of magmatic source. This hypothesis is supported by the similarity of the Nd isotopic compositions of the gabbros, monzonites and syenites. However, these rocks have undergone variable degrees of hydrothermal alteration, alkali metasomatism and contamination, which resulted in significant positive shifts of their Sr isotopic ratios. The Sr isotopic composition of the source region and parent magma will thus be approached using the less contaminated samples of the magmatic series, i.e. the oxide-gabbros.

The initial Sr isotopic compositions of the three oxide-gabbros samples are bracketed between 0.70357 and 0.70460 and likely reflect the $^{87}\text{Sr}/^{86}\text{Sr}$ value of the corresponding mantle source. These low initial Sr isotopic ratios seem to preclude any significant interaction of the mantle derived magmas with the crust. This conclusion is supported by the Th/Yb versus Ta/Yb diagram (Pearce, 1982; 1983), in which the gabbros plot within the field of uncontaminated basalts derived from enriched mantle source regions (Fig. 12), suggesting the involvement of subcontinental lithosphere or OIB source mantle in their petrogenesis. The initial ϵNd values vary from +1.6 to +4.1 in the mafic, intermediate and felsic rocks. The available Sr-Nd isotope data for the oxide-gabbros plot within the OIB field.

The enriched geochemical features of continental intraplate magmas like those of the CHA have been attributed to a combination of DMM or HIMU and EM1 and EM2 mantle components (Zhang et al., 2001; Cebria et al., 2000; Wagner et al., 2003). The CHA gabbros

and basalts have incompatible element ratios (Ba/Nb, La/Nb, Zr/Nb, Th/Nb) that overlap known EM2 component values (Fig. 13). In addition, the gabbros have high K/Nb, and low Ce/Pb ($2.6 < \text{Ce/Pb} < 6.6$) and U/Pb ($0.04 < \text{U/Pb} < 0.2$) (Table 1), similar to those of continental magmas generated from enriched mantle sources (e.g., Zhang et al., 2001; Cook et al., 2005).

5.5. Magma generation and tectonic implications

The CHA magmatism is strictly coeval with a red bed sedimentation indicating a general uplift of the Central High Atlas during the Late Jurassic-Early Cretaceous times, from the Bathonian to the Barremian, i.e. from 165 to 125 Ma (Haddoumi et al., 2008; Frizon de Lamotte et al., 2009). Recent restoration of palaeomagnetic data indicates that the CHA structures were initiated before the Late Cretaceous (Torres-Lopez et al., 2016). Accordingly the Late Jurassic-Early Cretaceous uplift has produced a major domal structure centred on the CHA and was accompanied by plutonism and halokinetic diapirism along NE anticlinal ridges (Michard et al., 2011; Saura et al., 2013; Torres-Lopez et al., 2016). Such a domal structure and the 40 Ma duration of the magmatic event are consistent with a mantle plume related activity. The location of CHA at the triple junction between the western High Atlas, the middle Atlas and the eastern High Atlas (Fig. 1A) could have been the site of small-scale mantle plume. The enriched signature observed in the studied rocks may be a feature of relatively shallow lithospheric mantle source regions. The low Ce/Pb and Nb/U ratios of the CHA magmatism could be inherited from an ancient enrichment of the lithospheric mantle by subduction-related metasomatism that occurred during an earlier orogeny, either Variscan (e.g. Essaifi et al., 2014) or Panafrican (e.g. Gasquet et al., 2005).

The transitional to moderately alkaline features of the CHA magmatism are consistent with an extensional tectonic activity. The identification of the sources of the magmas in the enriched mantle instead of the depleted mantle suggests a low rate of crustal extension and a great contribution from subcontinental lithospheric mantle sources to the partial melts. Accordingly, the Late Jurassic-Early Cretaceous is a period of relative tectonic quiescence that followed the onset of spreading in the Central Atlantic and eastward movement of the African plate (Brede et al., 1992), and during which melting of the lithospheric mantle was caused by adiabatic decompression, shallow mantle upwelling and uprise of asthenospheric material.

6. Conclusion

During a period of tectonic quiescence, from the Late Jurassic to the Early Cretaceous, asthenospheric mantle upwelling under the Central High Atlas induced crustal doming, adiabatic decompression and partial melting of enriched upper mantle sources. The latter process generated transitional to moderately alkaline basaltic melts that ascended within the upper continental crust where they formed crustal magmatic chambers at the boundary between the Palaeozoic basement and the Mesozoic cover. Cooling, crystal accumulation and *in situ* fractional crystallization within these magmatic chambers allowed formation of composite mafic and felsic intrusions composed of troctolites, olivine-gabbros, oxide-gabbros, monzonites and syenites. Salt diapirism of Triassic evaporite-bearing rocks allowed the still-cooling magmatic rocks to intrude mid Jurassic sequences along pre-existing subvertical faults. Hydrothermal alteration and crustal contamination were intense in the intrusions. The monzonites and syenites underwent alkali metasomatism and their Sr isotopic compositions were highly modified by interactions with Jurassic limestones. Both the magmatic Sr and Nd isotopic compositions have been preserved in the less altered gabbros. The initial Sr-Nd isotopic composition of the most depleted gabbros and the incompatible element ratios are consistent with generation from an enriched upper mantle similar to an ocean island basalt source.

Acknowledgements

Constructive comments and suggestions by A. Marzoli and an anonymous reviewer are highly appreciated. These reviews greatly improved presentation of data and discussion. We wish to thank L. Reisberg from CRPG-Nancy for providing the Sr-Nd isotope data used in this study. Thanks also to René Maury for critical readings of the manuscript. This work is a contribution to the project URAC 43.

References

Alibert, C., Michard, A., Albarède, F., 1983. The transition from alkali basalts to kimberlite: isotope and trace elements evidence from melilitites. *Contributions to Mineralogy and Petrology* 82, 176-86.

- 1 Armando, G., 1999. Intracontinental alkaline magmatism: Geology, Petrography, Mineralogy
2 and Geochemistry of the Jbel Hayim Massif (Central High Atlas-Morocco). *Mémoires de*
3 *Géologie de l'Université de Lausanne* 31, 1-106.
- 4 Bensalah, M. K., Youbi, N., Mata, J., Madeira, J., Martins, L., El Hachimi, H., Bertrand, H.,
5 Marzoli, A., Bellieni, G., Doblas, M., Font, E., Medina, F., Mahmoudi, A., Beraâouz, H.,
6 Miranda, R., Verati, C., De Min, A., Ben Abbou, M., Zayane, R., 2013. The Jurassic-
7 Cretaceous basaltic magmatism of the Oued El-Abid syncline (High Atlas, Morocco):
8 physical volcanology, geochemistry and geodynamic implications. *Journal of African Earth*
9 *Sciences* 81, 60–81
- 10 Beraâouz, E. H., 1995. Épisodes magmatiques associés au rift atlasique et ouverture de
11 l'Atlantique central, Unpub. Ph.D. thesis, University Hassan II, Casablanca.
- 12 Beraâouz, E. H., Bonin, B., 1993. Magmatisme alcalin intra-continental en contexte de
13 décrochement: le massif plutonique mésozoïque de Tirrhist, Haut Atlas (Maroc). *Comptes*
14 *Rendus de l'Académie des Sciences de Paris* 317, 647–53.
- 15 Beraâouz, E. H., Platevoet, B., Bonin, B., 1994. Le magmatisme mésozoïque du Haut Atlas
16 (Maroc) et l'ouverture de l'Atlantique Central. *Comptes Rendus de l'Académie des Sciences*
17 *de Paris* 318, 1079-85.
- 18 Bernard-Griffiths, J., Fourcade, S., Dupuy, C., 1991. Isotopic study (Sr, Nd, O and C) of
19 lamprophyres and associated dykes from Tamazert (Morocco): crustal contamination
20 processes and source characteristics. *Earth and Planetary Science Letters* 103, 190–99.
- 21 Bertrand, H., Dostal, J., Dupuy, C., 1982. Geochemistry of Early Mesozoic tholeiites from
22 Morocco. *Earth and Planetary Science Letters* 58, 225–39.
- 23 Berrahma, M., Hernandez, J., 1985. Nouvelles données sur le volcanisme trachytique
24 hyperalcalin du volcan du Siroua (Anti-Atlas, Maroc). *Comptes Rendus de l'Académie des*
25 *Sciences de Paris* 300, 863-68.
- 26 Berrahma, M., Delaloye, M., Faure-Muret, A., Rachdi, H. E., 1993. Premières données
27 géochronologiques sur le volcanisme alcalin de Jbel Saghro, Anti-Atlas, Maroc. *Journal of*
28 *African Earth Sciences* 17, 333-41.

- 1 Blackburn, T.J., Olsen, P.E., Bowring, S.A., McLean, N.M., Kent, D.V., Puffer, J., McHone,
2 G., Rasbury, E.T., Et-Touhami, M., 2013. Zircon U–Pb geochronology links the end- Triassic
3 extinction with the central Atlantic magmatic province. *Science* 340, 941–945.
- 4 Bosch, D., Maury, R.C., El Azzouzi, M., Bollinger, C., Bellon, H., Verdoux, P., 2014.
5 Lithospheric origin for Neogene-Quaternary Middle Atlas lavas (Morocco): clues from trace
6 elements and Sr-Nd-Pb-Hf isotopes. *Lithos* 205, 247-65.
- 7 Bouabdellah, M., Hoernle, K., Kchit, A., Duggen, S., Hauff, F., Klugel, A., Lowry, D.,
8 Beaudoin, G., 2010. Petrogenesis of the Eocene Tamazert Continental Carbonatites (Central
9 High Atlas, Morocco): implications for a common source for the Tamazert and Canary and
10 Cape Verde Island Carbonatites. *Journal of Petrology* 51, 1655–86.
- 11 Bouabdli, A., Dupuy, C., Dostal, J., 1988. Geochemistry of Mesozoic alkaline lamprophyres
12 and related rocks from the Tamazert massif, High Atlas (Morocco). *Lithos* 22, 43–58.
- 13 Brechbühler, Y.A., Bernasconi, R., Schaer, J. P., 1988. Jurassic sediments of the Central High
14 Atlas of Morocco: deposition, burial and erosion history. In *The Atlas System of Morocco*
15 (ed. V. Jacobshagen), pp. 139–68, Lecture Notes in Earth Sciences no. 15.
- 16 Brede, R., Hauptmann, M., Herbig, H.G., 1992. Plate tectonics and the intracratonic mountain
17 ranges in Morocco. The Mesozoic-Cenozoic development of the Central High Atlas and the
18 Middle Atlas. *Geologische Rundschau* 81, 127-141.
- 19 Caña, J., 1968. Roches éruptives basiques et minéralisations en plomb, zinc et strontium de la
20 région de Tirrhist (Haute Atlas de Midelt). *Notes et Mémoires du Service Géologique du*
21 *Maroc* 206, 7–30.
- 22 Cebria, J.M., Lopez-Ruiz, J., Doblas, M., Oyarzún, R., Hertogen, J., Benito, R., 2000.
23 Geochemistry of the Quaternary alkali basalts of Garrotxa (NE Volcanic Province, Spain): a
24 case of double enrichment of the mantle lithosphere. *Journal of Volcanology and Geothermal*
25 *Research* 102, 217–35.
- 26 Charriere, A., Haddoumi, H., Mojon, P.O., Ferriere, J., Cuhe, D., Zili, L., 2009. Mise en
27 évidence par ostracodes et charophytes de l'âge paléocène des dépôts discordants sur les rides
28 anticlinales de la région d'Imilchil (Haut Atlas, Maroc); conséquences paléogéographiques et
29 structurales. *Comptes Rendus Palevol* 8, 9–19.

- 1 Charrière, A., Ibouh, H., Haddoumi, H., 2011. Le Haut Atlas central de Beni Mellal à
2 Imilchil. In Nouveaux Guides géologiques et miniers du Maroc, volume 4 (eds. A. Michard,
3 O. Saddiqi, A. Chalouan, E.C., Rjimati, A. Mouttaqi), pp. 109-64. Notes et Mémoires du
4 Service Géologique du Maroc n° 559.
- 5 Charrière, A., Haddoumi, H., Mojon, P.O., 2005. Découverte du Jurassique supérieur et d'un
6 niveau marin du Barrémien dans les « Couches rouges » continentales du Haut Atlas central
7 marocain : implications paléogéographiques et structurales. *Comptes Rendus Palevol* 4, 385–
8 94.
- 9 Chèvremont, P., 1975. Les roches éruptives basiques des boutonnières de Tassent et Tasraft et
10 leurs indices métallifères dans leur cadre géologique (Haut-Atlas Central, Maroc). Unpub.
11 Ph.D. thesis, Univ. Claude Bernard, Lyon, 148 p.
- 12 Choulet, F., Charles, N., Barbanson, L., Branquet, Y., Sizaret, S., Ennaciri, A., Lakhlifi, B.,
13 Chen, Y., 2014. Non-sulfide zinc deposits of the Moroccan High Atlas: Multi-scale
14 characterization and origin. *Ore Geology Reviews* 56, 115–40.
- 15 Cook, C., Briggs, R.M., Smith, I.E.M., Maas, R., 2005. Petrology and geochemistry of
16 intraplate basalts in the South Auckland Volcanic Field, New Zealand: Evidence for two
17 coeval Magma suites from distinct sources. *Journal of Petrology* 46, 473-503.
- 18 Davies, J.H.F.L., Marzoli, A. Bertrand, H. Youbi, N., Ernest, M., Schaltegger, U., 2017. End-
19 Triassic mass extinction started by intrusive CAMP activity. *Nature Communications* 8, doi:
20 10.1038/ncomms15596
- 21 Dewey, J.F., Pitman, W.C., Ryan, W.B.J., 1973. Plate tectonics and the evolution of the
22 Alpine system. *Geological Society of America Bulletin* 84, 3137- 80.
- 23 Drummond, M.S., Ragland, P.C., Wesolowski, D., 1986. An example of trondhjemite genesis
24 by means of alkali metasomatism: Rockford Granite, Alabama Appalachians. *Contributions to*
25 *Mineralogy and Petrology* 93, 98–113.
- 26 Duggen, S., Hoernle, K.A., Hauff, F., Klügel, A., Bouabdellah, M., Thirlwall, M. F., 2009.
27 Flow of Canary mantle plume material through a subcontinental lithospheric corridor beneath
28 Africa to the Mediterranean. *Geology* 37, 283–86.

- 1 Dupuy, C., Dostal, J., 1984. Trace element geochemistry of some continental tholeiites. *Earth*
2 *and Planetary Science Letters* 67, 61–69.
- 3 El Azzouzi, M., Maury, R.C., Bellon, H., Youbi, N., Cotton, J., Kharbouch, F., 2010.
4 Petrology and K–Ar chronology of the Neogene–Quaternary Middle Atlas basaltic province,
5 Morocco. *Bulletin de la Société Géologique de France* 181, 243–57.
- 6 Elburg, M.A., Bons, P.D., Dougherty-Page, J., Janka, C.E., Neumann, N., Schaefer, B., 2001.
7 Age and metasomatic alteration of the Mt Neil granite at Nooldoonooldoona Waterhole, Mt
8 Painter inlier, South Australia. *Australian Journal Earth Sciences* 48, 721–30.
- 9 Ellouz, N., Patriat, M., Gaulier, J.-M., Bouatmani, R., Sabounji, S., 2003. From rifting to
10 Alpine inversion. Mesozoic and Cenozoic subsidence history of some Moroccan basins.
11 *Sedimentary Geology* 156, 185–212.
- 12 Essaifi, A. Samson, S., Goodenough, K., 2014. Geochemical and Sr-Nd isotopic constraints
13 on the petrogenesis and geodynamic significance of the Jebilet magmatism (Variscan Belt,
14 Morocco). *Geological Magazine* 151, 666-91
- 15 Ferrandini, M., Philip, J., Babinot, J.F., Ferrandini, J., Tronchetti, G., 1985. La plateforme
16 carbonatée du Cénomano-Turonien de la région d’Erfoud-Errachidia (Sud-Est marocain):
17 stratigraphie et paléoenvironnement. *Bulletin de la Société Géologique de France* 8, 559-64.
- 18 Fiechtner, L., Freidrichsen, H., Hammerschmidt, K., 1992. Geochemistry and geochronology
19 of Early Mesozoic tholeiites from Central Morocco. *Geologische Rundschau* 81, 45-62.
- 20 Fraissinet, C., Zouine, E., Morel, J.L., Poisson, A., Andrieux, J., Faure-Muret, A., 1988.
21 Structural evolution of the Southern and Northern Central High Atlas in Palaeocene and Mio-
22 Pliocene times. In *The Atlas system of Morocco* (ed. V.H. Jacobshagen), pp. 273-291,
23 *Lecture Notes in Earth Sciences* no. 15.
- 24 Frizon de Lamotte, D., Zizi, M., Missenard, Y., Hafid, M., El Azzouzi, M., Maury, R.C.,
25 Charriere, A., Taki, Z., Benammi, M., Michard, A., 2008. Chapter 4: the Atlas System. In
26 *Continental Evolution: The Geology of Morocco* (eds. A. Michard, O. Saddiqi, A. Chalouan,
27 D. Frizon Lamotte). pp. 116-33, *Lecture Notes in Earth Sciences* no. 116.

- 1 Frizon de Lamotte, D., Leturmy, P., Missenard, Y., Khomsi, S., Ruiz, G., Saddiqi, O.,
2 Guillocheau, F., Michard, A., 2009. Mesozoic and Cenozoic vertical movements in the Atlas
3 system (Algeria, Morocco, Tunisia): an overview. *Tectonophysics* 475, 9–28
- 4 Frost, B.R. Barnes, C.G., Collins, W.J. Arculus, R.J. Ellis, D.J., Frost, C.D., 2001. A
5 Geochemical Classification for Granitic Rocks. *Journal of Petrology* 42, 2033–48
- 6 Fulla, J., Fernández, M., Afonso, J.C., Vergès, J., Zeyen, H., 2010. The structure and
7 evolution of the lithosphere-asthenosphere boundary beneath the Atlantic-Mediterranean
8 Transition Region. *Lithos* 120, 74-95.
- 9 Gasquet, D., Levresse, G., Cheilletz, A., Azizi-Samir, M.R., Mouttaqi, A., 2005. Contribution
10 to a geodynamic reconstruction of the Anti-Atlas (Morocco) during Pan-African times with
11 the emphasis on inversion tectonics and metallogenic activity at the Precambrian–Cambrian
12 transition. *Precambrian Research* 140, 157–82.
- 13 Govindaraju, K., 1995. Working values with their confidence limits for twenty six CRPG,
14 ANRT and IWG-GIT geostandards. *Geostandards Newsletter* 19, 32pp.
- 15 Görler, K., Helmdach, F.F., Gaemers, P. Heissig, K. Hinsch, W., Mädler, K., Schwarzhaus,
16 W., Zucht, M., 1988. The uplift of the central High Atlas as deduced from Neogene
17 continental sediments of the Ouarzazate province, Morocco. In *The Atlas system of Morocco*
18 (ed. V.H. Jacobshagen), pp. 361-404, *Lecture Notes in Earth Sciences* no. 15.
- 19 Haddoumi, H., Charrière, A., Mojon, P.O., 2010. Stratigraphie et sédimentologie des
20 «Couches rouges» continentales du Jurassique-Crétacé du Haut Atlas central (Maroc):
21 implications paléogéographiques et géodynamiques. *Geobios* 43, 433-51.
- 22 Hart, S.D.R. Gerlach, D.C., White, W.M., 1986. A possible new Sr-Nd-Pb mantle array and
23 consequences for mantle mixing, *Geochimica et Cosmochimica Acta* 50, 1551-57.
- 24 Hernandez, J., Bellon, H., 1985. Chronologie K-Ar du volcanisme miocène du Rif oriental
25 (Maroc): implications tectoniques et magmatologiques. *Revue Géologie Dynamique et*
26 *Géographie Physique Paris* 262, 85-94.
- 27 Hollister, L.S., Grissom, G.C., Peters, E.K., Stowell, H.H., Sisson, V.B., 1987. Confirmation
28 of the empirical correlation of Al in hornblende with pressure of solidification of calc-alkaline
29 plutons. *American Mineralogist* 72, 231-39.

- 1 Ibouh, H., 2004. Du rift avorté au bassin sur décrochement, contrôles tectonique et
 2 sédimentaire pendant le Jurassique (Haut Atlas Central, Maroc). Unpub. Ph.D. thesis, Univ.
 3 Cadi Ayyad, Marrakech, 224 p.
- 4 Jacobshagen, V., Brede, R., Hauptmann, M., Heinitz, W., Zylka, R., 1988. Structure and post-
 5 Paleozoic evolution of the central High Atlas. In *The Atlas system of Morocco* (ed. V.H.
 6 Jacobshagen), pp. 245-71, Lecture Notes in Earth Sciences no. 15.
- 7 Jenny, J., Le Marrec, A., Monbaron, M., 1981. Les couches rouges du Jurassique moyen du
 8 Haut Atlas central (Maroc): corrélations lithostratigraphiques, éléments de datations et cadre
 9 tectono-sédimentaire, *Bulletin de la Société Géologique de France* XXIII, 627–39.
- 10 Kay, R.W., Gast, P.W., 1973. The rare earth content and origin of alkali-rich basalts, *Journal*
 11 *of Geology* 81, 653–82.
- 12 Knight, K.B., Nomade, S., Renne, P.R., Marzoli, A., Bertrand, H., Youbi, N., 2004. The
 13 Central Atlantic Magmatic Province at the Triassic–Jurassic boundary: paleomagnetic and
 14 $^{40}\text{Ar}/^{39}\text{Ar}$ evidence for brief, episodic volcanism. *Earth and Planetary Science Letters* 228,
 15 143–60.
- 16 Lanyon, R., Varne, R., Crawford, A.J., 1993. Tasmanian Tertiary basalts, the Balleny plume,
 17 and opening of the Tasman Sea (southwest Pacific Ocean). *Geology* 21, 555–58.
- 18 Laville, E., Piqué, A., 1992. Jurassic penetrative deformation and Cenozoic uplift in the
 19 central High Atlas (Morocco): a tectonic model. *Structural and Orogenic inversions*,
 20 *Geologische Rundsch* 81, 157–170
- 21 Laville, E., Zayane R., Honnorez, J., Piqué, A., 1994. Le métamorphisme jurassique du Haut
 22 Atlas central (Maroc); épisodes synschisteux et hydrothermaux. *Comptes Rendus de*
 23 *l'Académie des Sciences de Paris* 318, 1349–56.
- 24 Le Bas, M.J., Le Maitre, R.W., Streckeisen, A., Zanettin, B., 1986. A chemical classification
 25 of volcanic rocks based on the total alkali-silica diagram. *Journal of Petrology* 27, 745–50.
- 26 Lee, C.-T.A., Luf, P., Plank, T., Dalton, H., Leeman, W.P., 2009. Constraints on the depths
 27 and temperatures of basaltic magma generation on Earth and other terrestrial planets using
 28 new thermobarometers for mafic magmas. *Earth and Planetary Science Letters* 279, 20–33.

- 1 Leterrier, J., Maury, R.C., Thonon, P., Girard, D., Marchal, M., 1982. Clinopyroxene
2 composition as a method of identification of the magmatic affinities of paleo-volcanic series.
3 Earth and Planetary Science Letters 59, 139–54.
- 4 Lhachmi, A., 1992. Pétrologie de l'intrusion alcaline et des roches magmatiques associées de
5 la région d'Anemzi (Haut Atlas Central, Maroc). Unpub. Ph.D. thesis, Musée National
6 d'Histoire Naturelle, Paris, 153p.
- 7 Lhachmi, A., Lorand, J.P., Fabries, J., 2001. Pétrologie de l'intrusion alcaline mésozoïque de
8 la région d'Anemzi, Haut Atlas Central, Maroc. Journal of African Earth Sciences 32, 741-64.
- 9 Lorenz, J.C., 1988. Synthesis of Late Paleozoic and Triassic red bed sedimentation in
10 Morocco. In The Atlas system of Morocco (ed. V.H. Jacobshagen), pp.139-68, Lecture Notes
11 in Earth Sciences no. 15.
- 12 Lutz, T.M., Foland, K.A., Faul, H., Srogi, L., 1988. The strontium and oxygen isotopic record
13 of hydrothermal alteration of syenites from the Abu Khruq complex, Egypt. Contributions to
14 Mineralogy and Petrology 98, 212-23
- 15 Ma, G.S-K., Malpas, J., Suzuki, K., Lo, C-H., Wang, K-L., Iizuka, Y., Xenophontos, C.,
16 2013. Evolution and origin of the Miocene intraplate basalts on the Aleppo Plateau, NW
17 Syria. Chemical Geology 335, 149–71
- 18 Manspeizer, W., 1988. Triassic–Jurassic rifting and opening of the Atlantic; an overview. In
19 Triassic–Jurassic rifting, Continental Breakup and the Origin of the Atlantic Ocean and
20 Passive Margins (ed. W. Manspeizer), pp. 41–79. Developments in Geotectonics, Part A.
21 Elsevier, Amsterdam.
- 22 Manspeizer, W., Puffer, J. H., Cousmier, H. L., 1978. Separation of Morocco and Eastern
23 North America: a Triassic–Liassic stratigraphic record. Geological Society of America
24 Bulletin 89, 901–20.
- 25 Marzoli, A., Renne, P.R., Piccirillo, E.M., Ernesto, M., Bellieni, G., De Min, A., 1999.
26 Extensive 200-million-year-old continental flood basalts of the central Atlantic Magmatic
27 Province. Science 284, 616–18.
- 28 Marzoli, A., Bertrand, H., Knight, K.B., Cirilli, S., Vérati, C., Nomade, S., Martini, R., Youbi,
29 N., Allenbach, K., Neuwerth, R., Buratti, N., Rapaille, C., Zaninetti, L., Bellieni, G., Renne,

- 1 P. R., 2004. Synchrony of the Central Atlantic magmatic province and the Triassic–Jurassic
2 boundary climatic and biotic crisis. *Geology* 32, 973–76.
- 3 Mattauer, M. Tapponnier, P., Proust, F., 1977. Sur les mécanismes de formation des chaînes
4 intracontinentales. L'exemple des chaînes atlasiques du Maroc. *Bulletin de la Société*
5 *Géologique de France* XIX, 521–26
- 6 Mattis, A.F., 1977. Nonmarine Triassic sedimentation, Central High Atlas Mountains,
7 Morocco. *Journal of Sedimentary Petrology* 47, 107–19.
- 8 Maury, R.C., Fourcade, S., Coulon, C., El Azzouzi, M., Bellon, H., Coutelle, A., Ouabadi, A.,
9 Semroud, B., Megartsi, M., Cotten, J., Belanteur, O., Louni-Hacini, A., Piqué, A., Capdevila,
10 R., Hernandez, J., Réhault, J.-P., 2000. Postcollisional Neogene magmatism of the
11 Mediterranean Maghreb margin: a consequence of slab breakoff. *Comptes Rendus de*
12 *l'Académie des Sciences de Paris* 331, 159–73
- 13 Medina, F., 1995. Syn- and postrift evolution of the El Jadida–Agadir basin (Morocco):
14 constraints for the rifting model of the Central Atlantic. *Canadian Journal Earth Sciences* 32,
15 1273–91.
- 16 Michard, A., Ibouh, H., Charrière, A., 2011. Syncline-topped anticlinal ridges from the High
17 Atlas: a Moroccan conundrum, and inspiring structures from the Syrian Arc, Israel. *Terra*
18 *Nova* 23, 314–23.
- 19 Michard, A., Frizon de Lamotte, D. Hafid, M., Charrière, A., Haddoumi, H., Ibouh, H., 2013.
20 Comment on “The Jurassic–Cretaceous basaltic magmatism of the Oued El-Abid syncline
21 (High Atlas, Morocco): Physical volcanology, geochemistry and geodynamic implications”
22 by Bensalah et al., *J. Afr. Earth Sci.* 81 (2013), 60–81, *Journal of African Earth Sciences* 88,
23 101–05.
- 24 Missenard, Y., Zeyen, H., Frizon de Lamotte, D., Leturmy, P., Petit, C., Sébrier, M., Saddiqi,
25 O., 2006. Crustal versus asthenospheric origin of relief of the Atlas mountains of Morocco.
26 *Journal of Geophysical Research* 111, 1–13.
- 27 Missenard, Y., Cadoux, A., 2012. Can Moroccan Atlas lithospheric thinning and volcanism be
28 induced by Edge-Driven Convection? *Terra Nova* 24, 27–33.

- 1 Miyashiro, A., 1978. Nature of alkalic volcanic rock series. *Contributions to Mineralogy and*
- 2 *Petrology* 66, 91–104.
- 3 Mouguina, E.M., 2004. Les minéralisations polymétalliques (Zn–Pb, Cu, Co, Ni) du
- 4 Jurassique du Haut Atlas central (Maroc): Contexte géodynamique, typologies et modèles
- 5 génétiques. Unpub. Ph.D. thesis, Univ. Cadi Ayyad, Marrakech
- 6 Nomade, S., Knight, K.B., Beutel, E., Renne, P.R., Vérati, C., Féraud, G., Marzoli, A., Youbi,
- 7 N., Bertrand, H., 2007. Chronology of the Central Atlantic Magmatic Province: implications
- 8 for the Central Atlantic rifting processes and the Triassic–Jurassic biotic crisis.
- 9 *Palaeogeography, Palaeoclimatology, Palaeoecology* 244, 326–44
- 10 Otten, M.T., 1984. The origin of brown hornblende in the Artfjället gabbro and dolerites.
- 11 *Contributions to Mineralogy and Petrology* 86, 189–99.
- 12 Pearce, J.A., 1982. Trace element characteristics of lavas from destructive plate boundaries.
- 13 In *Orogenic Andesites* (ed. R.S. Thorpe), pp. 528–48, Wiley, Chichester, UK.
- 14 Pearce, J.A., 1983. The role of sub-continental lithosphere in magma genesis at destructive
- 15 plate margins. In *Continental Basalts and Mantle Xenoliths* (eds. C.J. Hawkesworth, M.J.
- 16 Norry), pp. 230–49. Nantwich: Shiva.
- 17 Price, R.C., Gray, C.M., Frey, F.A., 1997. Strontium isotopic and trace element heterogeneity
- 18 in the plains basalts of the Newer Volcanic Province, Victoria, Australia. *Geochimica et*
- 19 *Cosmochimica Acta* 61, 171–92.
- 20 Rachdi, H., Berrahma, M., Delalolye, M., Faure-Muret, A., Dahmani, M., 1997. Le
- 21 volcanisme tertiaire du Rekkame (Maroc): pétrologie, géochimie et géochronologie. *Journal*
- 22 *of African Earth Sciences* 24, 259–69.
- 23 Ragland P.C., 1989. *Basic analytical petrology*. Oxford university press. 369pp.
- 24 Richard, P., Shimizu, N., Allègre, C.J., 1976. $^{143}\text{Nd}/^{146}\text{Nd}$ a natural tracer: an application to
- 25 oceanic basalts. *Earth Planetary Science Letters* 31, 269–78.
- 26 Saddiqi, O., El Haimer, F. Z., Michard, A., Ruiz, G., Barbarand, J., Mansour, E.M., Leturmy,
- 27 P., Frizon de Lamotte, D., 2009. Apatite fission-track analyses on basement granites from
- 28 Western Meseta, Morocco: paleogeographic implications and interpretation of age
- 29 discrepancies. *Tectonophysics* 475, 22–30.

- 1 Saidi, A., 1992. Les processus de différenciation magmatique des complexes plutoniques
2 alcalins de la ride de Tasraft (Haut Atlas central) : pétrologie et structurologie. Unpub. 3rd
3 cycle thesis, Univ. Cadi Ayyad, Marrakech, 185 p.
- 4 Samuel, J., Rouault, R., Besnus, Y., 1985. Analyse multiélémentaire standardisée des
5 matériaux géologiques en spectrométrie d'émission par plasma par couplage inductif.
6 *Analyst* 13, 312-17.
- 7 Saunders, A.D., Norry, M.J., Tarney, J., 1988. Origin of MORB and chemically depleted
8 mantle reservoirs: trace element constraints. *Journal of Petrology*, Special Lithosphere Issue,
9 415–45.
- 10 Sebai, A., Feraud, G., Bertrand, H., Hanes, J., 1991. $^{40}\text{Ar}/^{39}\text{Ar}$ dating and geochemistry of
11 tholeiitic magmatism related to the early opening of the Central Atlantic rift. *Earth and*
12 *Planetary Science Letters* 104, 455-72.
- 13 Saura, E., Vergés, J., Martin-Martin, J.D., Messenger, G., Moragas, M., Razin, P., Grelaud, C.,
14 Joussiaume, R., Malaval, M., Homke, S., Hunt, D.W., 2014. Syn- to post-rift diapirism and
15 minibasins of the Central High Atlas (Morocco): the changing face of a mountain belt. *Journal*
16 *of the Geological Society*, London 171, 97–105.
- 17 Shellnutt, J.G., Zhou, M.-F., Zellmer, G.F., 2009. The role of Fe–Ti oxide crystallization in
18 the formation of A-type granitoids with implications for the Daly gap: An example from the
19 Permian Baima igneous complex, SW China. *Chemical Geology* 259, 204–17
- 20 Souhel, A., 1996. Le mésozoïque dans le Haut Atlas de Béni Mellal (Maroc). *Stratigraphie,*
21 *sédimentologie et évolution géodynamique*, *Strata* 2, 1–249.
- 22 Souhel, A., Canérot, J., 1989. Polarités sédimentaires téthysienne puis atlantique: l'exemple
23 des couches rouges jurassico-crétacées du Haut Atlas central (Maroc). *Sciences Géologiques*
24 *Mémoires* 83, 39–46.
- 25 Studer, M.A., 1980. Métamorphisme d'enfouissement dans le Haut-Atlas Central (Maroc).
26 Essai sur l'évolution de l'épaisseur des couvertures sédimentaires. *Comptes Rendus de*
27 *l'Académie des Sciences de Paris* 291, 457-60.

- 1 Sun, S.S., McDonough, W.F., 1989. Chemical and isotopic systematics of oceanic basalts:
2 implications of mantle composition and processes, in *Magmatism in Ocean Basins* (eds. A.D.
3 Saunders, M.J. Norry), pp. 313–45. Geological Society of London, Special Publication no. 42.
- 4 Teixell, A., Ayarza, P., Zeyen, H., Fernàndez, M., Arboleya, M.L., 2005. Effects of mantle
5 upwelling in a compressional setting: the Atlas Mountains of Morocco. *Terra Nova* 17, 456-
6 61.
- 7 Torres-Lopez, S., Casas, A.M., Villalín J.J., El Ouardi, H., Moussaid, B., 2016, Pre-
8 Cenomanian vs. Cenozoic folding in the High Atlas revealed by palaeomagnetic data. *Terra*
9 *Nova* 28, 110-19.
- 10 Vérati, C., Rapaille, C., Féraud, G., Marzoli, A., Bertrand, H., Youbi, N., 2007. $^{40}\text{Ar}/^{39}\text{Ar}$ ages
11 and duration of the Central Atlantic Magmatic Province volcanism in Morocco and Portugal
12 and its relation to the Triassic–Jurassic boundary. *Palaeogeography, Palaeoclimatology,*
13 *Palaeoecology* 244, 308–25.
- 14 Wagner, C., Mokhtari, A., Deloule, E., Chabaux, F., 2003. Carbonatite and alkaline
15 magmatism in Taourirt (Morocco): petrological, geochemical and Sr–Nd isotope
16 characteristics. *Journal of Petrology* 44, 937-65.
- 17 Wass, S.Y., 1979. Multiple origin of clinopyroxene in alkali basaltic rocks. *Lithos* 12, 115-32.
- 18 Weaver, B.L., 1991a. The origin of ocean island basalts end-member compositions: trace
19 element and isotopic constraints. *Earth and Planetary Science Letters* 104, 381–97.
- 20 Weaver, B.L., 1991b. Trace element evidence for the origin of ocean island basalts. *Geology*
21 19, 123–26.
- 22 Wilson, M., 1993. Geochemical signatures of continental and oceanic basalts: a key to mantle
23 dynamics? *Journal of the Geological Society, London* 150, 977–90.
- 24 Winchester, J.A., Floyd, P.A., 1976. Geochemical magma type discrimination: application to
25 altered and metamorphosed basic igneous rocks. *Earth and Planetary Science Letters* 28, 459–
26 69.
- 27 Youbi, N., Martins, L., Munhá, J.M., Ibouh, H., Madeira, J., Aït Chayeb, E.H., El Boukhari,
28 A., 2003. The Late Triassic–Early Jurassic Volcanism of Morocco and Portugal in the
29 framework of the Central Atlantic Magmatic Province. In “The Central Atlantic Magmatic

- Province: Insights from Fragments of Pangea” (eds. W.E. Hame, J.M. McHone, P.R. Renne, C. Ruppel), pp. 179–207, Geophysical Monographs Series 136.
- Zayane, R., 1992. La série plutonique du Haut Atlas central marocain (région d’Imilchil) : pétrographie et géochimie ; aspects métamorphiques et structuraux de sa mise en place. Unpub. Ph.D. thesis, Univ. Bretagne occidentale, Brest.
- Zayane, R., Saidi, A., Essaifi, A., Bouabdelli, M., 2001. Minéralogie des altérations hydrothermales des intrusions jurassiques du Haut Atlas central (Maroc). Notes et Mémoires Service Géologique Maroc 408, 108-19.
- Zayane, R., 2002. Magmatisme intraplaque et hydrothermalisme associé : le cas du Haut Atlas central (Maroc). Unpub. Ph.D. thesis, Cadi Ayyad University, Marrakech.
- Zayane, R., Essaifi, A., Maury, R.C., Piqué, A., Laville, E., Bouabdelli, M., 2002. Cristallisation fractionnée et contamination crustale dans la série magmatique jurassique transitionnelle du Haut Atlas central (Maroc). Comptes Rendus Geosciences 334, 97–104.
- Zhang, M., Stephenson, P.J., O’Reilly, S.Y., McCulloch, M.T., Norman, M., 2001. Petrogenesis and geodynamic implications of late Cenozoic basalts in North Queensland, Australia: trace element and Sr–Nd–Pb isotope evidence. Journal of Petrology 42, 685–719.
- Zindler, A., Hart, S., 1986. Chemical geodynamics. Annual Review of Earth and Planetary Sciences 14, 493–571.

Figure Captions

Figure. 1. Geological setting of the Central High Atlas Late Jurassic-Early Cretaceous magmatism

(A) North-West Africa map showing the location of the CHA magmatic province (modified after Missenard and Cadoux, 2011). Also indicated are the locations of Cenozoic alkaline volcanism outcrops. Periods of volcanic activity are compiled from Wagner et al. (2003) for Taourirt, Bouabdellah et al. (2010) for Tamazert, Hernandez and Bellon (1985) for Gourougou, Oujda and Guilliz, Rachdi et al. (1997) for Rekkame, El Azzouzi et al. (2010) for the Middle Atlas, Berrahma and Hernandez (1985) and Berrahma et al. (1993) for Sarrhro and Siroua. The area overlying an anomalously-thin lithosphere zone is shown in grey.

(B) Geological map of the Imilchil area showing Tasraft, Tassent and Tirrhist anticlinal ridges, with location of Figs. 2 and 3.

Figure. 2. Vertical cross section through the Tasraft and Tassent ridges (see location in Fig. 1b) showing the intrusions and the related magmatic chambers located at the bottom of the Mesozoic cover.

Figure. 3. Geological map of the Tirrhist intrusion (modified from Beraâouz, 1995). Location of the Sr-Nd samples is indicated.

Figure. 4 (colour online). Field and thin section photos illustrating the Central High Atlas intrusive magmatism. (A) Field view of the Tassent anticlinal ridge showing the contact between Middle Jurassic sediments and the layered basic-ultrabasic intrusion, (B) Field view of a syenitic megadyke in the Jbel Hayim massif, (C) Metre-scale syenitic dyke cross-cutting hydrothermally altered gabbro in the Tirrhist intrusion, (D) centimetre-scale layering in the mafic-ultramafic cumulates, (E) Olivine-gabbro with olivine (Ol), poekilitic clinopyroxene (Cpx), plagioclase (Pl), and biotite (Bi), (F) Oxide-gabbro with plagioclase (Pl), hornblende (Hbl), and titanomagnetite (op); Note the albitization rims (Ab) around plagioclase, (G) micrographic texture with alkali feldspar (Afs) and quartz (Qz) developed around K-feldspar (Kfs) in the syenite, (H) K-feldspar (Kfs) and plagioclase (Pl) surrounded by albite rims (Ab) in the syenite.

Figure. 5 Binary plots for selected major (A, wt%) and trace elements (B, ppm) of the CHA plutonic rocks against MgO (wt %). Black square (troctolite), white circle (olivine-gabbro), black circle (oxide-gabbro), multiply sign (microgabbro). Grey circle (hydrothermally altered gabbro), white triangle (monzonite), plus sign (syenite). The scatter of data points in the hydrothermally altered gabbros and syenites is related to postmagmatic remobilization of K, Na, Rb and Ba.

Figure. 6 Total alkalis vs. silica (TAS diagram, after Le Bas et al., 1986) for the CHA plutonic rocks with subalkaline-alkaline fields after Miyashiro (1978). Symbols as in Fig. 5.

Figure. 7 Plots of the CHA intrusives in the classification diagrams of Frost et al. (2001). (A) $\text{FeO}^*/(\text{FeO}^*+\text{MgO})$ versus SiO_2 showing the boundary between the magnesian and the ferroan rocks, (B) $\text{Na}_2\text{O}+\text{K}_2\text{O}-\text{CaO}$ versus SiO_2 showing the boundaries between calcic, calc-alkalic, alkali-calcic and alkalic granitoids. Symbols as in Fig. 5.

Figure. 8 (colour online). Chondrite-normalized rare earth element patterns of the CHA plutonic rocks and basalts. (A) oxide-gabbros and hydrothermally altered gabbro, (B) monzonites, (C) syenites, (D) superposition of the REE fields of the CHA plutonic and volcanic rocks. Normalizing values from McDonough and Sun (1995). The original data for the basalts are from Bensalah et al. (2013).

Figure. 9 (colour online). Primitive mantle-normalized trace element patterns for the CHA plutonic rocks and basalts. (A) oxide-gabbros and hydrothermally altered gabbro, (B) monzonites, (C) syenites, (D) superposition of the spider-diagram fields of the CHA plutonic and volcanic rocks. Normalizing values from Sun and McDonough (1989). The original data for the basalts are from Bensalah et al. (2013).

Figure. 10 (colour online). Initial $^{87}\text{Sr}/^{86}\text{Sr}$ vs. initial ϵNd plots for the CHA plutonic rocks. The HIMU (mantle with high $^{238}\text{U}/^{204}\text{Pb}$ ratio) mantle reservoir end-member composition is from Zindler and Hart (1986). The original data for the Eocene Tamazert alkaline rocks from Bernard-Griffiths et al. (1991) and Bouabdellah et al. (2010) are also plotted. The hyperbola

in (b) indicates mixing between the less contaminated gabbro sample and Jurassic limestone. Numbers along the hyperbola indicate the mixing parameter f . Mixing parameters for the limestone are respectively 1000 ppm and 2 ppm for Sr and Nd concentrations, 0.708000 and 0.512450 for Sr and Nd isotope ratios. Data sources: from Bouabdellah et al. (2010).

Figure. 11 Variation diagrams for incompatible trace element abundance (ppm) in the gabbroic rocks (filled circles) and monzonitic to syenitic rocks (crosses) of the CHA intrusives. Some element ratios (e.g. Y/Nb, La/Nb) show a significant variation in the magmatic series.

Figure. 12 (colour online). Plot of the CHA intrusive rocks in the Th/Yb versus Ta/Yb diagram (after Pearce, 1983). Vectors shown indicate the influence of subduction components (S), within-plate enrichment (W), crustal contamination (C) and fractional crystallization (F). Dashed lines separate the boundaries of the tholeiitic (TH), calc-alkaline (CA) and shoshonitic (SH) fields. Filled circles (gabbros) crosses (monzonites and syenites).

Figure. 13 (colour online). Plots of Zr/Nb, La/Nb, Th/Nb and Ba/Nb against K/Nb illustrating the geochemical characteristics of the mantle sources for CHA Late Jurassic- Early Cretaceous magmatism compared with the HIMU, EMI, and EMII mantle reservoirs of Zindler and Hart (1986). The fields for HIMU, EMI, and EMII are based on data compiled from Saunders et al. (1988), Weaver (1991a, 1991b), and Lanyon et al. (1993).

1 Table 1, Major (wt%) and trace element (ppm) data of representative samples from the
 2 intrusive rocks of the Central High Atlas Magmatic Province.

Rock type	TRC	TRC	TRC	OLG	OLG	OLG	OLG	OLG	OXG	OXG	OXG
Sample	88-49*	87-25*	87-55*	87-68*	87-60*	87-72*	88-93*	88-56*	TR8	TR9	TR10
Location	Tassen	Tassen	Tirrhist	Tirrhist	Tirrhist	Tirrhist	Tassen	Tasraft	Tirrhist	Tirrhist	Tirrhist
SiO ₂	44.1	44.83	46.41	47.71	48.35	48.19	48.8	50.9	47.2	46.8	47.7
TiO ₂	0.83	0.97	1.15	1.53	1.7	1.54	0.88	1.43	3	3	2.83
Al ₂ O ₃	10.8	11	14.05	14.77	15.29	15.7	18.2	16.8	16.4	14.3	17.4
Fe ₂ O ₃	15.5	14.64	12.61	11.99	11.37	11.38	9.8	11	13.8	14.7	12.5
MnO	0.2	0.19	0.17	0.16	0.16	0.17	0.17	0.16	0.18	0.169	0.14
MgO	19	17.49	12.13	9.84	8.26	8.33	7.6	7.08	4.62	4.68	4.51
CaO	4.8	6.13	7.39	8.11	8.45	8.82	9.3	7.9	10.05	10.09	10.73
Na ₂ O	1.83	2.2	2.87	3.34	3.6	3.3	3.21	3.71	3.55	3.29	3.8
K ₂ O	0.66	0.59	0.56	0.89	0.99	0.88	0.62	0.98	0.84	0.75	0.65
P ₂ O ₅	0.19	0.16	0.16	0.24	0.24	0.19	0.24	0.27	0.25	0.19	0.13
LOI	0.46	0.9	1.8	0.4	0.4	0.7	0.53	0.4	0.46	0.12	0.3
total	98.37	99.1	99.3	98.98	98.81	99.2	99.35	100.63	100.35	98.089	100.69
Sc	10.8	†	†	†	†	†	18.9	19.7	29.4	34.8	31.1
V	115	109	127	165	180	172	137	188	423	523	510
Cr	770	808	455	334	292	282	148	258	34	119	33
Co	104	†	†	†	†	†	38.4	42	56	60	52
Ni	566	535	398	246	182	191	148	158	43	46	42
Cu	105	87	46	50	48	57	48.5	40.9	114	130	114
Zn	134	107	100	103	111	163	101	95	129	126	91
Ga	†	14	18	19	24	22	†	†	†	†	†
Rb	†	13	8	8	11	14	†	†	9.87	9.13	6.47
Sr	265	300	354	434	425	432	411	385	539	388	574
Y	8.4	12	13	18	17	16	10.9	18	18.7	18.1	15
Zr	61.8	80	89	129	137	112	55.1	106	98	82	69
Nb	9.2	10	12	16	17	14	9.6	11.8	†	†	†
Cs	†	†	†	†	†	†	†	†	0.48	0.58	0.53
Ba	83.9	95	102	123	140	134	77.6	125	113	103	99
Hf	†	†	†	†	†	†	†	†	2.69	2.52	1.98
Ta	†	†	†	†	†	†	†	†	0.98	0.92	0.69
Pb	†	†	†	†	†	†	†	†	4.09	6.91	5.86
La	†	†	†	†	†	†	3.5	8.8	10.08	8.60	7.40
Ce	†	†	†	†	†	†	15.3	18	21.15	18.68	15.49
Pr	†	†	†	†	†	†	†	†	2.84	2.53	2.10
Nd	†	†	†	†	†	†	†	†	13.14	12.21	9.68
Sm	†	†	†	†	†	†	†	†	3.72	3.67	2.80
Eu	†	†	†	†	†	†	†	†	1.47	1.43	1.23
Gd	†	†	†	†	†	†	†	†	3.68	3.56	2.77
Tb	†	†	†	†	†	†	†	†	0.66	0.67	0.51
Dy	†	†	†	†	†	†	†	†	3.68	3.84	3.03
Ho	†	†	†	†	†	†	†	†	0.77	0.74	0.59
Er	†	†	†	†	†	†	†	†	1.83	1.79	1.38
Tm	†	†	†	†	†	†	†	†	0.24	0.25	0.20
Yb	0.5	†	†	†	†	†	0.8	1.5	1.57	1.62	1.25
Lu	†	†	†	†	†	†	0.1	†	0.24	0.25	0.18
Th	†	6	2	†	1	5	†	†	1.27	1.01	0.77
U	†	†	†	†	†	†	†	†	0.68	0.30	0.35
Ce/Pb									5.17	2.70	2.64
U/Pb									0.17	0.04	0.06

1 Table 1 (Continued)

Rock type	OXG	OXG	OXG	OXG	MCG	MCG	HAG	HAG	HAG	HAG	HAG
Sample	TR11	TR12	88-78*	88-134*	88-100*	88-120*	TR48	88-29*	86-6*	88-53*	88-50*
Location	Tirrhis	Tirrhis	Tasraft	Tassent	Tassent	Tasraft	Tasraft	Tassent	Tassent	Tasraft	Tassen
SiO ₂	47.3	48.3	47.8	49	50.7	51.4	48.9	48.4	49.9	50.1	48.3
TiO ₂	2.93	2.45	2.12	1.77	1.95	1.56	2.12	1.19	1.57	1.31	1.15
Al ₂ O ₃	17.5	17.7	15.8	15.9	16	15.3	16.6	16	16	14.2	13.6
Fe ₂ O ₃	13.2	12.1	11.8	12	5.7	6.9	11.4	10.8	9.8	10.1	11.5
MnO	0.145	0.132	0.19	0.12	0.14	0.06	0.213	0.14	0.12	0.14	0.12
MgO	4.53	5.01	4.57	4.53	8.04	7.76	5.37	8.69	6.63	10	10.2
CaO	10.74	11.04	8.8	9.8	6.3	9.9	10.14	7.9	9.5	6	5.5
Na ₂ O	3.54	3.51	3.75	3.85	2.71	3.86	2.71	2.9	3.47	2.85	2.9
K ₂ O	0.64	0.61	1.12	0.8	3.62	0.81	1.57	0.69	0.87	1.55	1.41
P ₂ O ₅	0.11	0.08	0.32	0.31	0.39	0.23	0.13	0.22	0.22	0.24	0.18
LOI	0.21	0.18	1.82	2.41	3.26	3.06	1.56	1.73	2.54	4.45	3.58
total	100.85	101.11	98.09	100.49	98.81	100.84	100.713	98.66	100.62	100.94	98.44
Sc	31.3	32.8	26.6	26.3	23.6	17.7	31.4	18.2	19.5	31	31.8
V	540	561	265	262	193	156	396	172	170	265	253
Cr	45	63	128	143	218	202	65	294	229	333	594
Co	56	54	31.3	43.9	29.6	25.7	43	49.1	39.3	50.6	50.1
Ni	46	61	42.5	57.8	158	172	41	211	151	162	188
Cu	136	170	57.9	94.2	6.8	3.8	66	46.7	13.7	3.8	7.4
Zn	101	83	74.2	56.2	88	44.6	105	61.9	53	265	1406
Ga	†	†	†	†	†	†	†	†	19	†	†
Rb	6.73	6.51	†	†	†	†	33.83	†	25	†	†
Sr	589	463	813	583	1261	795	436	362	488	140	108
Y	13.8	12.8	21.8	17.5	22.4	20.9	12.3	13	17.1	22.4	18.3
Zr	71	60	138	71.5	150	131	62	73.4	86.4	129	98.8
Nb	†	†	15.8	3.9	17.9	14.8	†	8.7	7.4	9.9	7.2
Cs	0.39	0.34	†	†	†	†	0.93	†	†	†	†
Ba	95	80	133	75.4	991	108	354	91	122	145	80.7
Hf	1.92	1.80	†	†	†	†	1.42	†	†	†	†
Ta	0.51	0.58	†	†	†	†	0.52	†	†	†	†
Pb	5.76	2.12	†	†	†	†	6.55	†	†	†	†
La	7.17	6.45	8.5	8.8	18	11.7	7.63	†	†	12.3	5.1
Ce	14.78	14.01	31.1	12.4	51.6	40.6	15.84	†	†	40.3	†
Pr	2.02	1.88	†	†	†	†	2.04	†	†	†	†
Nd	9.18	9.06	†	†	†	†	8.93	†	†	†	†
Sm	2.64	2.67	†	†	†	†	2.47	†	†	†	†
Eu	1.21	1.14	†	†	†	†	1.09	†	†	†	†
Gd	2.48	2.47	†	†	†	†	2.42	†	†	†	†
Tb	0.47	0.46	†	†	†	†	0.42	†	†	†	†
Dy	2.75	2.70	†	†	†	†	2.37	†	†	†	†
Ho	0.56	0.54	†	†	†	†	0.48	†	†	†	†
Er	1.33	1.28	†	†	†	†	1.08	†	†	†	†
Tm	0.18	0.18	†	†	†	†	0.16	†	†	†	†
Yb	1.15	1.10	1.9	1.4	1.7	1.5	0.88	0.8	1.3	2	1.4
Lu	0.17	0.16	†	†	0.1	0.1	0.15	0.1	0.1	†	†
Th	0.91	0.74	†	†	†	†	0.84	†	†	†	†
U	0.32	0.24	†	†	†	†	0.24	†	†	†	†
Ce/Pb	2.56	6.61					2.42				
U/Pb	0.06	0.11					0.04				

2
3

4

1 Table 1 (Continued)

Rock type	HAG	HAG	HAG	MNZ	MNZ	SYN	SYN	SYN	SYN	SYN	SYN
Sample	87-65*	88-51*	88-55*	TS4	TR2	TR25	TR21	TR24	TR32	TR33	TR34
Location	Tirrhist	Tasse	Tassent	Tasraf	Tirrhist	Tirrhis	Tirrhis	Tirrhis	Tirrhis	Tirrhis	Tirrhis
SiO ₂	49.01	49.6	51	56.5	57.1	61.4	63.6	61	64.1	67.1	65.9
TiO ₂	1.64	1.06	1.23	0.82	1.14	0.79	0.74	1.12	0.25	0.18	0.31
Al ₂ O ₃	16.3	13.8	14.2	15.7	16.9	16.3	18.4	17.7	16.4	16.8	16.7
Fe ₂ O ₃	9.77	10.6	10	13.7	7.4	8.6	1.7	6.7	6.8	4.6	4.4
MnO	0.14	0.14	0.06	0.034	0.079	0.112	0.018	0.068	0.034	0.032	0.031
MgO	5.73	10.7	10.9	1.02	1.04	0.38	0.8	0.62	0.12	0.13	0.15
CaO	9.76	7.3	2.3	2.27	4.77	1.38	2.93	2.06	0.51	0.52	0.55
Na ₂ O	3.45	3.01	3.99	7.68	8.64	7.18	9.73	7.89	6.84	6.84	6.79
K ₂ O	1.32	0.92	0.1	0.72	0.49	3.53	0.86	2.59	4.14	4.62	4.62
P ₂ O ₅	0.22	0.19	0.25	0.2	0.3	0.12	0.16	0.15	0.02	0.01	0.02
LOI	2.8	3.33	4.58	0.13	2.96	0.57	1.64	0.35	0.78	0.33	0.61
total	100.14	100.65	98.61	98.77	100.82	100.36	100.58	100.25	99.99	101.2	100.1
Sc	†	29.5	32.5	7.4	7.7	4.8	5.3	5.1	0.3	0.3	0.4
V	22	243	275	174	17	2	18	6	0	0	1
Cr	291	529	327	0	1	13	1	1	0	0	21
Co	†	49.5	36	15	19	8	9	12	3	2	2
Ni	58	206	130	12	11	1	6	1	0	27	0
Cu	64	55.7	33.2	13	5	2	10	5	0	0	1
Zn	71	52.7	59.4	27	13	49	60	38	41	34	34
Ga	19	†	†	†	†	†	†	†	†	†	†
Rb	22	†	†	7.12	3.42	26.82	6.12	18.89	31.47	39.47	37.62
Sr	644	173	35.1	88	880	243	271	347	61	49	43
Y	19	18.2	21	39	36.5	36.2	46.3	40.5	63.8	32	46.7
Zr	120	100	129	286	259	215	262	329	781	224	512
Nb	16	7.3	9.9	†	†	†	†	†	†	†	†
Cs	†	†	†	0.08	0.06	0.21	0.10	0.13	0.21	0.21	0.20
Ba	153	50.3	7.8	108	98	471	239	355	136	141	130
Hf	†	†	†	6.31	6.51	5.29	6.68	8.83	12.91	5.06	9.56
Ta	†	†	†	2.12	2.13	2.46	2.72	3.19	2.39	1.82	2.84
Pb	†	†	†	10.64	2.87	1.79	13.07	1.91	1.58	1.62	1.69
La	†	5.7	†	26.14	21.83	35.35	44.96	26.91	41.45	24.00	25.69
Ce	†	16.1	†	53.25	49.68	68.38	91.57	53.72	80.84	46.52	51.28
Pr	†	†	†	6.41	6.30	8.71	10.54	6.79	9.40	5.38	6.09
Nd	†	†	†	26.60	27.57	36.26	41.22	28.15	36.50	21.32	24.32
Sm	†	†	†	6.87	6.92	8.64	9.21	7.51	9.37	5.35	6.25
Eu	†	†	†	2.44	4.40	3.36	2.29	2.62	1.04	0.75	0.81
Gd	†	†	†	6.29	6.41	7.50	8.20	6.70	9.00	4.80	6.01
Tb	†	†	†	1.12	1.17	1.40	1.50	1.26	1.71	0.94	1.19
Dy	†	†	†	6.73	6.61	7.92	8.77	7.61	10.85	5.79	7.52
Ho	†	†	†	1.43	1.33	1.62	1.74	1.61	2.42	1.20	1.68
Er	†	†	†	3.42	3.42	3.89	4.51	4.06	6.23	2.85	4.21
Tm	†	†	†	0.50	0.47	0.57	0.66	0.59	1.04	0.46	0.68
Yb	†	1.5	1.7	2.83	3.17	3.66	4.00	3.81	6.08	2.74	4.09
Lu	†	†	†	0.45	0.51	0.59	0.65	0.61	1.02	0.48	0.70
Th	†	†	†	4.53	4.33	2.98	3.75	5.83	7.20	3.21	4.48
U	†	†	†	1.48	2.05	0.94	1.58	1.84	2.55	0.95	1.71
Ce/Pb				5.01	17.31	38.15	7.01	28.19	51.19	28.71	30.27
U/Pb				0.14	0.72	0.52	0.12	0.97	1.62	0.59	1.01

2

3 Table 1 (Continued)

Rock type	SYN	SYN	SYN	SYN	SYN	SYN	SYN	SYN	SYN	SYN
Sample	TS3	TS6	87-45*	88-136*	87-66*	88-137*	86-8*	88-139*	88-138*	87-53*
Location	Tirrhist	Tirrhist	Tassen	Tassen	Tirrhist	Tassen	Tirrhist	Tassen	Tassen	Tasraft
SiO ₂	62.8	65.5	62.4	64.4	66.7	66.5	68.2	68.6	71.3	62.5
TiO ₂	0.66	0.42	0.62	0.55	0.22	0.74	0.72	0.37	0.35	0.64
Al ₂ O ₃	14.7	18.2	16.6	15.5	17	14.9	15.5	14.4	14.7	17.4
Fe ₂ O ₃	11.8	3.3	5.7	2.7	4.2	7.4	4.4	7.5	1.6	6
MnO	0.042	0.006	0.13	0.02	0.03	0.05	0.04	0.02	0.02	0.08
MgO	0.2	0.43	0.37	1.89	0.25	0.15	0.47	0.08	0.1	0.65
CaO	1.16	1.21	0.9	2.4	0.4	1	1	0.3	0.4	1.7
Na ₂ O	6.61	9.3	6.96	7.71	6.72	6.76	7.89	6.73	7.09	6.25
K ₂ O	1.97	0.75	3.53	0.34	4.61	2.69	1.12	2.03	2.02	4.2
P ₂ O ₅	0.11	0.08	0.22			0.19	0.2			0.18
LOI	0.25	0.25	1.3	2.79	0.44	0.36	0.7	0.38	0.62	0.72
total	100.302	99.446	98.73	98.3	100.57	100.74	100.24	100.41	98.2	100.32
Sc	6.4	2	4.9	3.8	1.7	7.9	7.2	1.8	1.9	6.2
V	3	7	4.7	30.2	2.3	6.5	13	6.3	9.6	6.2
Cr	0	0	6.9	8.4	8.6	7.7	1.9	11.2	5.7	3
Co	10	6	7	9.6	6.5	10.5	17.1	7.9	5.2	7.8
Ni	309	4	19.5	3.2	22.1	8.4	7.3	3.8	†	10.8
Cu	25	0	5.8	2.8	4.6	3.7	23.2	15.8	4.2	14.7
Zn	22	3	173	51.2	19.8	22.5	36.2	53.5	54.3	48.8
Ga	†	†	†	†	†	†	28	†	†	†
Rb	18.48	9.43	†	†	†	†	10	†	†	†
Sr	114	762	114	77.1	103	264	126	71.3	83.5	592
Y	49.4	28	41.2	72.8	34.2	70	45.9	53.2	70.9	33.8
Zr	470	349	330	472	244	340	434	739	691	343
Nb	†	†	52.5	50.2	30.1	75	35	34.6	74.5	24.5
Cs	0.14	0.12	†	†	†	†	†	†	†	†
Ba	340	65	317	62.9	209	675	203	183	184	615
Hf	10.10	6.94	†	†	†	†	†	†	†	†
Ta	2.60	2.35	†	†	†	†	†	†	†	†
Pb	3.30	0.97	†	†	†	†	†	†	†	†
La	29.39	27.78	32.5	40.7	13.9	40.5	40.8	25.6	25.9	24.2
Ce	56.78	57.12	77.7	116	48.8	99.3	59.5	80.5	77.8	62
Pr	6.52	6.35	†	†	†	†	†	†	†	†
Nd	26.35	23.35	†	†	†	†	†	†	†	†
Sm	6.98	5.20	†	†	†	†	†	†	†	†
Eu	1.82	0.83	†	†	†	†	†	†	†	†
Gd	7.03	4.52	†	†	†	†	†	†	†	†
Tb	1.30	0.78	†	†	†	†	†	†	†	†
Dy	8.11	4.55	†	†	†	†	†	†	†	†
Ho	1.74	0.95	†	†	†	†	†	†	†	†
Er	4.33	2.45	†	†	†	†	†	†	†	†
Tm	0.66	0.39	†	†	†	†	†	†	†	†
Yb	3.72	2.40	3.5	5.9	3.1	6	4.6	5.2	5.9	3.4
Lu	0.64	0.41	0.2	0.9	0.3	0.7	0.3	0.3	0.9	0.2
Th	7.89	5.90	†	†	†	†	3	†	†	†
U	2.62	2.06	†	†	†	†	†	†	†	†
Ce/Pb	17.20	58.71								
U/Pb	0.79	2.11								

^aTotal Fe as Fe₂O₃; † not available; TRC (troctolite), OLG (olivine-gabbro), OXG (oxide-gabbro), MCG (microgabbro), HAG (hydrothermally altered gabbro), MNZ (Monzonite), SYN (syenite).

Table 2, Rb, Sr, Sm and Nd concentrations (ppm), Sr and Nd isotopic ratios of the intrusive rocks of the Tirrhist intrusion (For locations see Fig. 3)

Rock type	Sample	Rb	Sr	$^{87}\text{Rb}/^{86}\text{Sr}$	$^{87}\text{Sr}/^{86}\text{Sr}$	$\pm 2\sigma$	$(^{87}\text{Sr}/^{86}\text{Sr})_i$	Sm	Nd	$^{147}\text{Sm}/^{144}\text{Nd}$	$^{143}\text{Nd}/^{144}\text{Nd}$	$\pm 2\sigma$	ϵNd
Ox-Gabbro	TR8	9,87	539	0,053043	0,704715	15	0,704602	3,72	13,14	0,171892	0,512793	17	3,5
Ox-Gabbro	TR9	9,13	388	0,068143	0,703719	7	0,703574	3,67	12,21	0,182092	0,512814	5	3,7
Ox-Gabbro	TR10	6,47	574	0,032661	0,704416	22	0,704346	2,80	9,68	0,175237	0,512788	9	3,3
HA-Gabbro	TR48	33,83	436	0,224687	0,705285	19	0,704806	2,47	8,93	0,167502	0,512712	12	2,0
Monzonite	TR2	3,42	880	0,011253	0,707498	13	0,707474	6,92	27,57	0,152127	0,512678	8	1,6
Syenite	TR21	6,12	271	0,065380	0,707071	21	0,706932	9,21	41,22	0,135451	0,512722	2	2,8
Syenite	TR25	26,82	243	0,319632	0,707401	21	0,706720	8,64	36,26	0,144576	0,512799	17	4,1
Syenite	TR32	31,47	61	1,493786	0,710250	13	0,707067	9,37	36,50	0,155704	0,512789	12	3,7

Ox-gabbro (oxide gabbro), HA-Gabbro (hydrothermally altered gabbro)

Table 1, Major (wt%) and trace element (ppm) data of representative samples from the intrusive rocks of the Central High Atlas Magmatic Province.

Rock type	TRC	TRC	TRC	OLG	OLG	OLG	OLG	OLG	OXG	OXG	OXG
Sample	88-49*	87-25*	87-55*	87-68*	87-60*	87-72*	88-93*	88-56*	TR8	TR9	TR10
Location	Tassen	Tassen	Tirrhist	Tirrhist	Tirrhist	Tirrhist	Tassen	Tasraft	Tirrhist	Tirrhist	Tirrhist
SiO ₂	44.1	44.83	46.41	47.71	48.35	48.19	48.8	50.9	47.2	46.8	47.7
TiO ₂	0.83	0.97	1.15	1.53	1.7	1.54	0.88	1.43	3	3	2.83
Al ₂ O ₃	10.8	11	14.05	14.77	15.29	15.7	18.2	16.8	16.4	14.3	17.4
Fe ₂ O ₃	15.5	14.64	12.61	11.99	11.37	11.38	9.8	11	13.8	14.7	12.5
MnO	0.2	0.19	0.17	0.16	0.16	0.17	0.17	0.16	0.18	0.169	0.14
MgO	19	17.49	12.13	9.84	8.26	8.33	7.6	7.08	4.62	4.68	4.51
CaO	4.8	6.13	7.39	8.11	8.45	8.82	9.3	7.9	10.05	10.09	10.73
Na ₂ O	1.83	2.2	2.87	3.34	3.6	3.3	3.21	3.71	3.55	3.29	3.8
K ₂ O	0.66	0.59	0.56	0.89	0.99	0.88	0.62	0.98	0.84	0.75	0.65
P ₂ O ₅	0.19	0.16	0.16	0.24	0.24	0.19	0.24	0.27	0.25	0.19	0.13
LOI	0.46	0.9	1.8	0.4	0.4	0.7	0.53	0.4	0.46	0.12	0.3
total	98.37	99.1	99.3	98.98	98.81	99.2	99.35	100.63	100.35	98.089	100.69
Sc	10.8	†	†	†	†	†	18.9	19.7	29.4	34.8	31.1
V	115	109	127	165	180	172	137	188	423	523	510
Cr	770	808	455	334	292	282	148	258	34	119	33
Co	104	†	†	†	†	†	38.4	42	56	60	52
Ni	566	535	398	246	182	191	148	158	43	46	42
Cu	105	87	46	50	48	57	48.5	40.9	114	130	114
Zn	134	107	100	103	111	163	101	95	129	126	91
Ga	†	14	18	19	24	22	†	†	†	†	†
Rb	†	13	8	8	11	14	†	†	9.87	9.13	6.47
Sr	265	300	354	434	425	432	411	385	539	388	574
Y	8.4	12	13	18	17	16	10.9	18	18.7	18.1	15
Zr	61.8	80	89	129	137	112	55.1	106	98	82	69
Nb	9.2	10	12	16	17	14	9.6	11.8	†	†	†
Cs	†	†	†	†	†	†	†	†	0.48	0.58	0.53
Ba	83.9	95	102	123	140	134	77.6	125	113	103	99
Hf	†	†	†	†	†	†	†	†	2.69	2.52	1.98
Ta	†	†	†	†	†	†	†	†	0.98	0.92	0.69
Pb	†	†	†	†	†	†	†	†	4.09	6.91	5.86
La	†	†	†	†	†	†	3.5	8.8	10.08	8.60	7.40
Ce	†	†	†	†	†	†	15.3	18	21.15	18.68	15.49
Pr	†	†	†	†	†	†	†	†	2.84	2.53	2.10
Nd	†	†	†	†	†	†	†	†	13.14	12.21	9.68
Sm	†	†	†	†	†	†	†	†	3.72	3.67	2.80
Eu	†	†	†	†	†	†	†	†	1.47	1.43	1.23
Gd	†	†	†	†	†	†	†	†	3.68	3.56	2.77
Tb	†	†	†	†	†	†	†	†	0.66	0.67	0.51
Dy	†	†	†	†	†	†	†	†	3.68	3.84	3.03
Ho	†	†	†	†	†	†	†	†	0.77	0.74	0.59
Er	†	†	†	†	†	†	†	†	1.83	1.79	1.38
Tm	†	†	†	†	†	†	†	†	0.24	0.25	0.20
Yb	0.5	†	†	†	†	†	0.8	1.5	1.57	1.62	1.25
Lu	†	†	†	†	†	†	0.1	†	0.24	0.25	0.18
Th	†	6	2	†	1	5	†	†	1.27	1.01	0.77
U	†	†	†	†	†	†	†	†	0.68	0.30	0.35
Ce/Pb									5.17	2.70	2.64
U/Pb									0.17	0.04	0.06

Table 1 (Continued)

Rock type	OXG	OXG	OXG	OXG	MCG	MCG	HAG	HAG	HAG	HAG	HAG
Sample	TR11	TR12	88-78*	88-134*	88-100*	88-120*	TR48	88-29*	86-6*	88-53*	88-50*
Location	Tirrhis	Tirrhis	Tasraft	Tassent	Tassent	Tasraft	Tasraft	Tassent	Tassent	Tasraft	Tassen
SiO ₂	47.3	48.3	47.8	49	50.7	51.4	48.9	48.4	49.9	50.1	48.3
TiO ₂	2.93	2.45	2.12	1.77	1.95	1.56	2.12	1.19	1.57	1.31	1.15
Al ₂ O ₃	17.5	17.7	15.8	15.9	16	15.3	16.6	16	16	14.2	13.6
Fe ₂ O ₃	13.2	12.1	11.8	12	5.7	6.9	11.4	10.8	9.8	10.1	11.5
MnO	0.145	0.132	0.19	0.12	0.14	0.06	0.213	0.14	0.12	0.14	0.12
MgO	4.53	5.01	4.57	4.53	8.04	7.76	5.37	8.69	6.63	10	10.2
CaO	10.74	11.04	8.8	9.8	6.3	9.9	10.14	7.9	9.5	6	5.5
Na ₂ O	3.54	3.51	3.75	3.85	2.71	3.86	2.71	2.9	3.47	2.85	2.9
K ₂ O	0.64	0.61	1.12	0.8	3.62	0.81	1.57	0.69	0.87	1.55	1.41
P ₂ O ₅	0.11	0.08	0.32	0.31	0.39	0.23	0.13	0.22	0.22	0.24	0.18
LOI	0.21	0.18	1.82	2.41	3.26	3.06	1.56	1.73	2.54	4.45	3.58
total	100.85	101.11	98.09	100.49	98.81	100.84	100.713	98.66	100.62	100.94	98.44
Sc	31.3	32.8	26.6	26.3	23.6	17.7	31.4	18.2	19.5	31	31.8
V	540	561	265	262	193	156	396	172	170	265	253
Cr	45	63	128	143	218	202	65	294	229	333	594
Co	56	54	31.3	43.9	29.6	25.7	43	49.1	39.3	50.6	50.1
Ni	46	61	42.5	57.8	158	172	41	211	151	162	188
Cu	136	170	57.9	94.2	6.8	3.8	66	46.7	13.7	3.8	7.4
Zn	101	83	74.2	56.2	88	44.6	105	61.9	53	265	1406
Ga	†	†	†	†	†	†	†	†	19	†	†
Rb	6.73	6.51	†	†	†	†	33.83	†	25	†	†
Sr	589	463	813	583	1261	795	436	362	488	140	108
Y	13.8	12.8	21.8	17.5	22.4	20.9	12.3	13	17.1	22.4	18.3
Zr	71	60	138	71.5	150	131	62	73.4	86.4	129	98.8
Nb	†	†	15.8	3.9	17.9	14.8	†	8.7	7.4	9.9	7.2
Cs	0.39	0.34	†	†	†	†	0.93	†	†	†	†
Ba	95	80	133	75.4	991	108	354	91	122	145	80.7
Hf	1.92	1.80	†	†	†	†	1.42	†	†	†	†
Ta	0.51	0.58	†	†	†	†	0.52	†	†	†	†
Pb	5.76	2.12	†	†	†	†	6.55	†	†	†	†
La	7.17	6.45	8.5	8.8	18	11.7	7.63	†	†	12.3	5.1
Ce	14.78	14.01	31.1	12.4	51.6	40.6	15.84	†	†	40.3	†
Pr	2.02	1.88	†	†	†	†	2.04	†	†	†	†
Nd	9.18	9.06	†	†	†	†	8.93	†	†	†	†
Sm	2.64	2.67	†	†	†	†	2.47	†	†	†	†
Eu	1.21	1.14	†	†	†	†	1.09	†	†	†	†
Gd	2.48	2.47	†	†	†	†	2.42	†	†	†	†
Tb	0.47	0.46	†	†	†	†	0.42	†	†	†	†
Dy	2.75	2.70	†	†	†	†	2.37	†	†	†	†
Ho	0.56	0.54	†	†	†	†	0.48	†	†	†	†
Er	1.33	1.28	†	†	†	†	1.08	†	†	†	†
Tm	0.18	0.18	†	†	†	†	0.16	†	†	†	†
Yb	1.15	1.10	1.9	1.4	1.7	1.5	0.88	0.8	1.3	2	1.4
Lu	0.17	0.16	†	†	0.1	0.1	0.15	0.1	0.1	†	†
Th	0.91	0.74	†	†	†	†	0.84	†	†	†	†
U	0.32	0.24	†	†	†	†	0.24	†	†	†	†
Ce/Pb	2.56	6.61					2.42				
U/Pb	0.06	0.11					0.04				

Table 1 (Continued)

Rock type	HAG	HAG	HAG	MNZ	MNZ	SYN	SYN	SYN	SYN	SYN	SYN
Sample	87-65*	88-51*	88-55*	TS4	TR2	TR25	TR21	TR24	TR32	TR33	TR34
Location	Tirrhist	Tasse	Tassent	Tasraf	Tirrhist	Tirrhis	Tirrhis	Tirrhis	Tirrhis	Tirrhis	Tirrhis
SiO ₂	49.01	49.6	51	56.5	57.1	61.4	63.6	61	64.1	67.1	65.9
TiO ₂	1.64	1.06	1.23	0.82	1.14	0.79	0.74	1.12	0.25	0.18	0.31
Al ₂ O ₃	16.3	13.8	14.2	15.7	16.9	16.3	18.4	17.7	16.4	16.8	16.7
Fe ₂ O ₃	9.77	10.6	10	13.7	7.4	8.6	1.7	6.7	6.8	4.6	4.4
MnO	0.14	0.14	0.06	0.034	0.079	0.112	0.018	0.068	0.034	0.032	0.031
MgO	5.73	10.7	10.9	1.02	1.04	0.38	0.8	0.62	0.12	0.13	0.15
CaO	9.76	7.3	2.3	2.27	4.77	1.38	2.93	2.06	0.51	0.52	0.55
Na ₂ O	3.45	3.01	3.99	7.68	8.64	7.18	9.73	7.89	6.84	6.84	6.79
K ₂ O	1.32	0.92	0.1	0.72	0.49	3.53	0.86	2.59	4.14	4.62	4.62
P ₂ O ₅	0.22	0.19	0.25	0.2	0.3	0.12	0.16	0.15	0.02	0.01	0.02
LOI	2.8	3.33	4.58	0.13	2.96	0.57	1.64	0.35	0.78	0.33	0.61
total	100.14	100.65	98.61	98.77	100.82	100.36	100.58	100.25	99.99	101.2	100.1
Sc	†	29.5	32.5	7.4	7.7	4.8	5.3	5.1	0.3	0.3	0.4
V	22	243	275	174	17	2	18	6	0	0	1
Cr	291	529	327	0	1	13	1	1	0	0	21
Co	†	49.5	36	15	19	8	9	12	3	2	2
Ni	58	206	130	12	11	1	6	1	0	27	0
Cu	64	55.7	33.2	13	5	2	10	5	0	0	1
Zn	71	52.7	59.4	27	13	49	60	38	41	34	34
Ga	19	†	†	†	†	†	†	†	†	†	†
Rb	22	†	†	7.12	3.42	26.82	6.12	18.89	31.47	39.47	37.62
Sr	644	173	35.1	88	880	243	271	347	61	49	43
Y	19	18.2	21	39	36.5	36.2	46.3	40.5	63.8	32	46.7
Zr	120	100	129	286	259	215	262	329	781	224	512
Nb	16	7.3	9.9	†	†	†	†	†	†	†	†
Cs	†	†	†	0.08	0.06	0.21	0.10	0.13	0.21	0.21	0.20
Ba	153	50.3	7.8	108	98	471	239	355	136	141	130
Hf	†	†	†	6.31	6.51	5.29	6.68	8.83	12.91	5.06	9.56
Ta	†	†	†	2.12	2.13	2.46	2.72	3.19	2.39	1.82	2.84
Pb	†	†	†	10.64	2.87	1.79	13.07	1.91	1.58	1.62	1.69
La	†	5.7	†	26.14	21.83	35.35	44.96	26.91	41.45	24.00	25.69
Ce	†	16.1	†	53.25	49.68	68.38	91.57	53.72	80.84	46.52	51.28
Pr	†	†	†	6.41	6.30	8.71	10.54	6.79	9.40	5.38	6.09
Nd	†	†	†	26.60	27.57	36.26	41.22	28.15	36.50	21.32	24.32
Sm	†	†	†	6.87	6.92	8.64	9.21	7.51	9.37	5.35	6.25
Eu	†	†	†	2.44	4.40	3.36	2.29	2.62	1.04	0.75	0.81
Gd	†	†	†	6.29	6.41	7.50	8.20	6.70	9.00	4.80	6.01
Tb	†	†	†	1.12	1.17	1.40	1.50	1.26	1.71	0.94	1.19
Dy	†	†	†	6.73	6.61	7.92	8.77	7.61	10.85	5.79	7.52
Ho	†	†	†	1.43	1.33	1.62	1.74	1.61	2.42	1.20	1.68
Er	†	†	†	3.42	3.42	3.89	4.51	4.06	6.23	2.85	4.21
Tm	†	†	†	0.50	0.47	0.57	0.66	0.59	1.04	0.46	0.68
Yb	†	1.5	1.7	2.83	3.17	3.66	4.00	3.81	6.08	2.74	4.09
Lu	†	†	†	0.45	0.51	0.59	0.65	0.61	1.02	0.48	0.70
Th	†	†	†	4.53	4.33	2.98	3.75	5.83	7.20	3.21	4.48
U	†	†	†	1.48	2.05	0.94	1.58	1.84	2.55	0.95	1.71
Ce/Pb				5.01	17.31	38.15	7.01	28.19	51.19	28.71	30.27
U/Pb				0.14	0.72	0.52	0.12	0.97	1.62	0.59	1.01

Table 1 (Continued)

Rock type	SYN	SYN	SYN	SYN	SYN	SYN	SYN	SYN	SYN	SYN
Sample	TS3	TS6	87-45*	88-136*	87-66*	88-137*	86-8*	88-139*	88-138*	87-53*
Location	Tirrhist	Tirrhist	Tassent	Tassent	Tirrhist	Tassent	Tirrhist	Tassent	Tassent	Tasraft
SiO ₂	62,8	65,5	62,4	64,4	66,7	66,5	68,2	68,6	71,3	62,5
TiO ₂	0,66	0,42	0,62	0,55	0,22	0,74	0,72	0,37	0,35	0,64
Al ₂ O ₃	14,7	18,2	16,6	15,5	17	14,9	15,5	14,4	14,7	17,4
Fe ₂ O ₃	11,8	3,3	5,7	2,7	4,2	7,4	4,4	7,5	1,6	6
MnO	0,042	0,006	0,13	0,02	0,03	0,05	0,04	0,02	0,02	0,08
MgO	0,2	0,43	0,37	1,89	0,25	0,15	0,47	0,08	0,1	0,65
CaO	1,16	1,21	0,9	2,4	0,4	1	1	0,3	0,4	1,7
Na ₂ O	6,61	9,3	6,96	7,71	6,72	6,76	7,89	6,73	7,09	6,25
K ₂ O	1,97	0,75	3,53	0,34	4,61	2,69	1,12	2,03	2,02	4,2
P ₂ O ₅	0,11	0,08	0,22			0,19	0,2			0,18
LOI	0,25	0,25	1,3	2,79	0,44	0,36	0,7	0,38	0,62	0,72
total	100,3	99,45	98,73	98,3	100,6	100,7	100,2	100,4	98,2	100,3
Sc	6,4	2	4,9	3,8	1,7	7,9	7,2	1,8	1,9	6,2
V	3	7	4,7	30,2	2,3	6,5	13	6,3	9,6	6,2
Cr	0	0	6,9	8,4	8,6	7,7	1,9	11,2	5,7	3
Co	10	6	7	9,6	6,5	10,5	17,1	7,9	5,2	7,8
Ni	309	4	19,5	3,2	22,1	8,4	7,3	3,8	†	10,8
Cu	25	0	5,8	2,8	4,6	3,7	23,2	15,8	4,2	14,7
Zn	22	3	173	51,2	19,8	22,5	36,2	53,5	54,3	48,8
Ga	†	†	†	†	†	†	28	†	†	†
Rb	18,48	9,43	†	†	†	†	10	†	†	†
Sr	114	762	114	77,1	103	264	126	71,3	83,5	592
Y	49,4	28	41,2	72,8	34,2	70	45,9	53,2	70,9	33,8
Zr	470	349	330	472	244	340	434	739	691	343
Nb	†	†	52,5	50,2	30,1	75	35	34,6	74,5	24,5
Cs	0,14	0,12	†	†	†	†	†	†	†	†
Ba	340	65	317	62,9	209	675	203	183	184	615
Hf	10,10	6,94	†	†	†	†	†	†	†	†
Ta	2,60	2,35	†	†	†	†	†	†	†	†
Pb	3,30	0,97	†	†	†	†	†	†	†	†
La	29,39	27,78	32,5	40,7	13,9	40,5	40,8	25,6	25,9	24,2
Ce	56,78	57,12	77,7	116	48,8	99,3	59,5	80,5	77,8	62
Pr	6,52	6,35	†	†	†	†	†	†	†	†
Nd	26,35	23,35	†	†	†	†	†	†	†	†
Sm	6,98	5,20	†	†	†	†	†	†	†	†
Eu	1,82	0,83	†	†	†	†	†	†	†	†
Gd	7,03	4,52	†	†	†	†	†	†	†	†
Tb	1,30	0,78	†	†	†	†	†	†	†	†
Dy	8,11	4,55	†	†	†	†	†	†	†	†
Ho	1,74	0,95	†	†	†	†	†	†	†	†
Er	4,33	2,45	†	†	†	†	†	†	†	†
Tm	0,66	0,39	†	†	†	†	†	†	†	†
Yb	3,72	2,40	3,5	5,9	3,1	6	4,6	5,2	5,9	3,4
Lu	0,64	0,41	0,2	0,9	0,3	0,7	0,3	0,3	0,9	0,2
Th	7,89	5,90	†	†	†	†	3	†	†	†
U	2,62	2,06	†	†	†	†	†	†	†	†
Ce/Pb	17,20	58,71								
U/Pb	0,79	2,11								

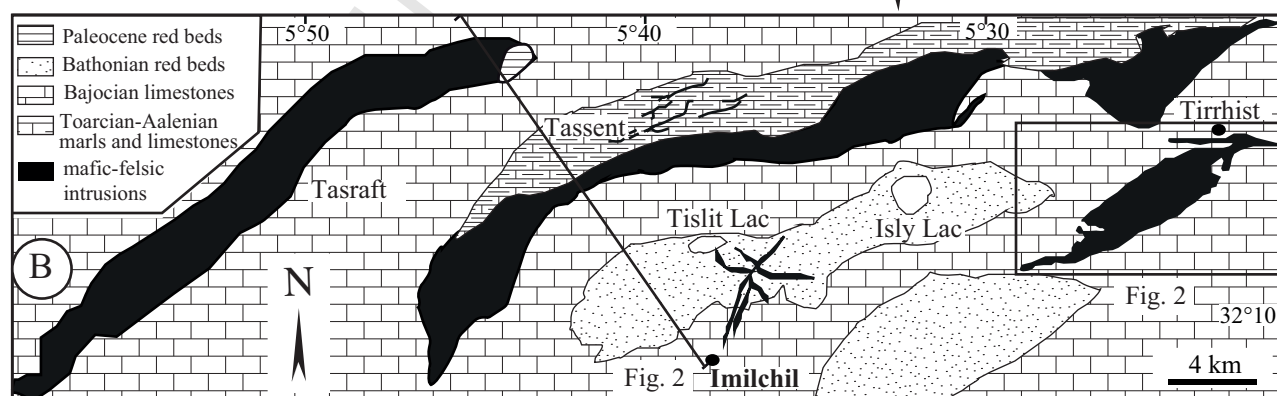
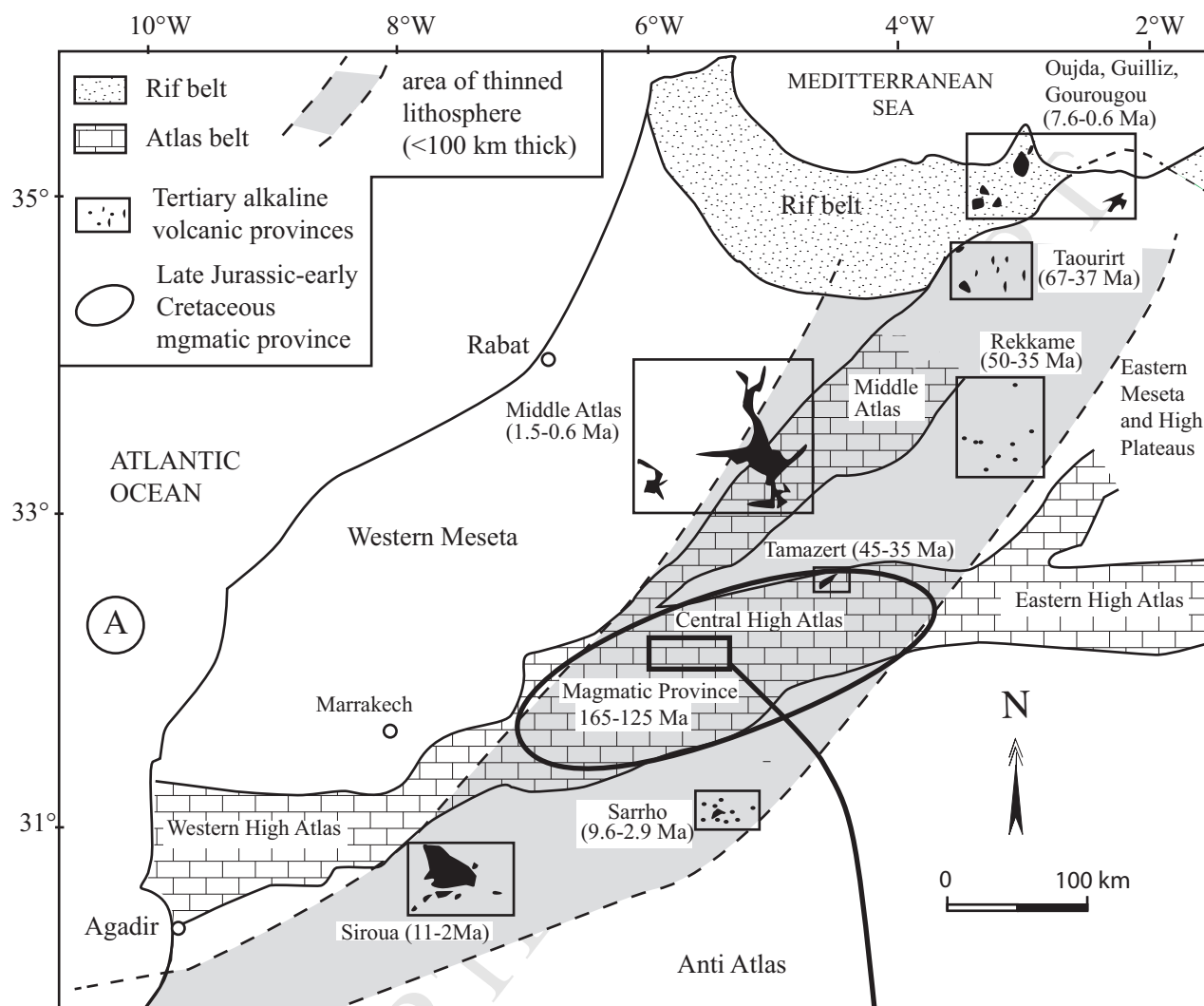
^aTotal Fe as Fe₂O₃; † not available; TRC (troctolite), OLG (olivine-gabbro), OXG (oxide-

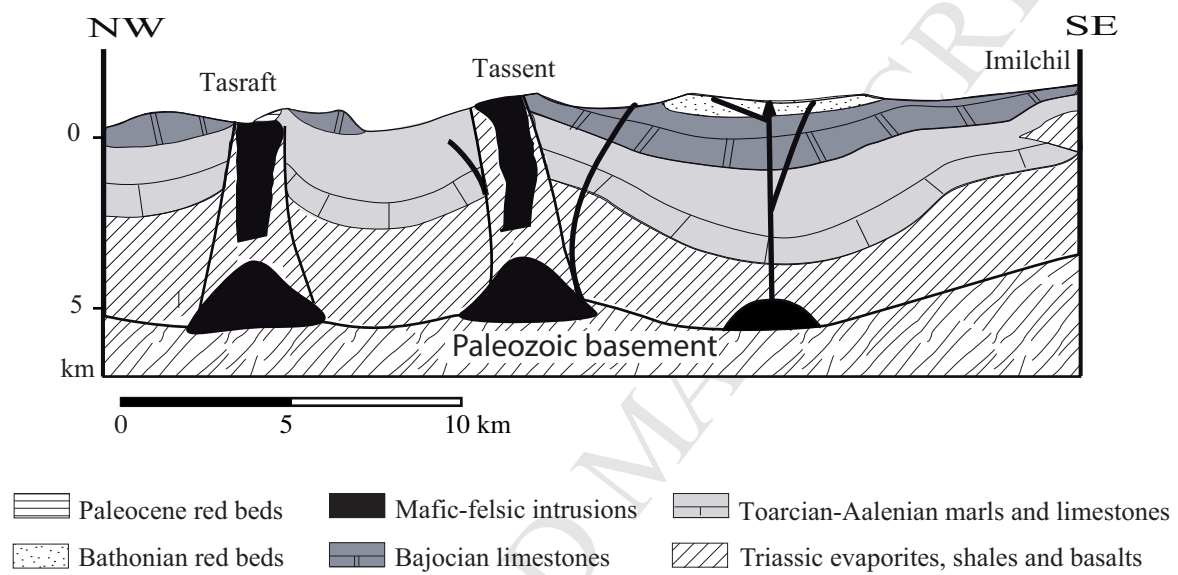
gabbro), MCG (microgabbro), HAG (hydrothermally altered gabbro), MNZ (Monzonite), SYN (syenite).

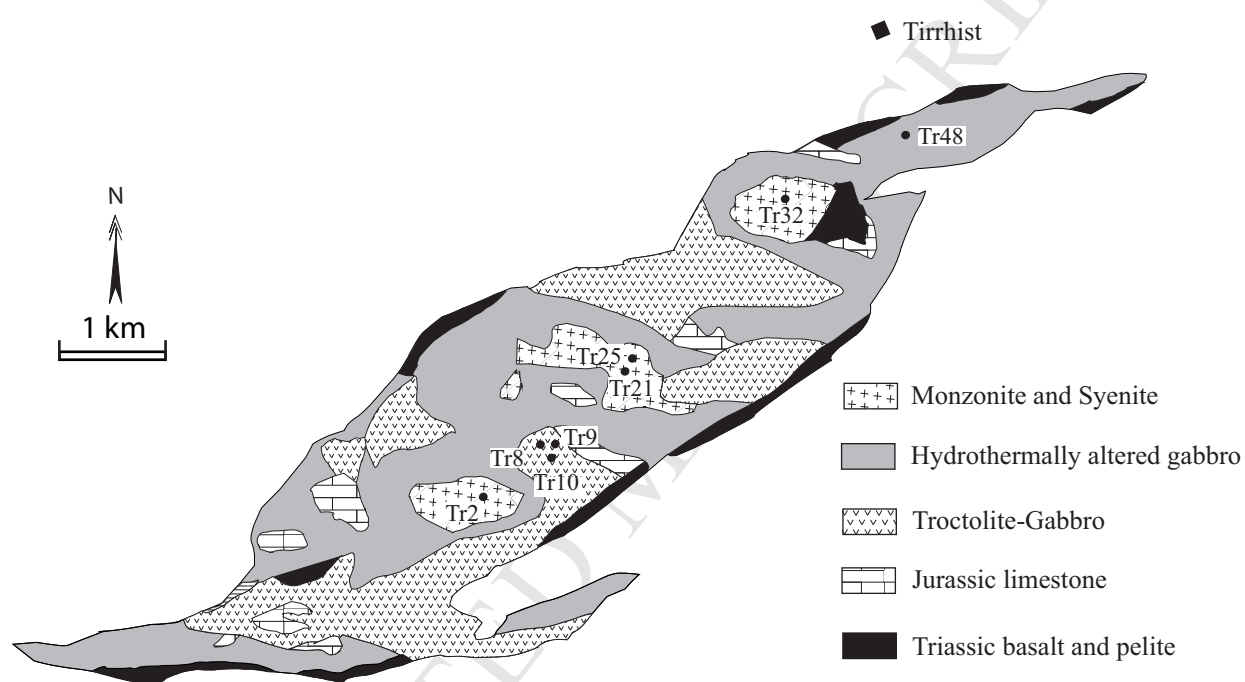
ACCEPTED MANUSCRIPT

Table 2, Rb, Sr, Sm and Nd concentrations (ppm), Sr and Nd isotopic ratios of the intrusive rocks of the Tirrhist intrusion (For locations see Fig. 3). Ox-gabbro (oxide gabbro), HA-Gabbro (hydrothermally altered gabbro).

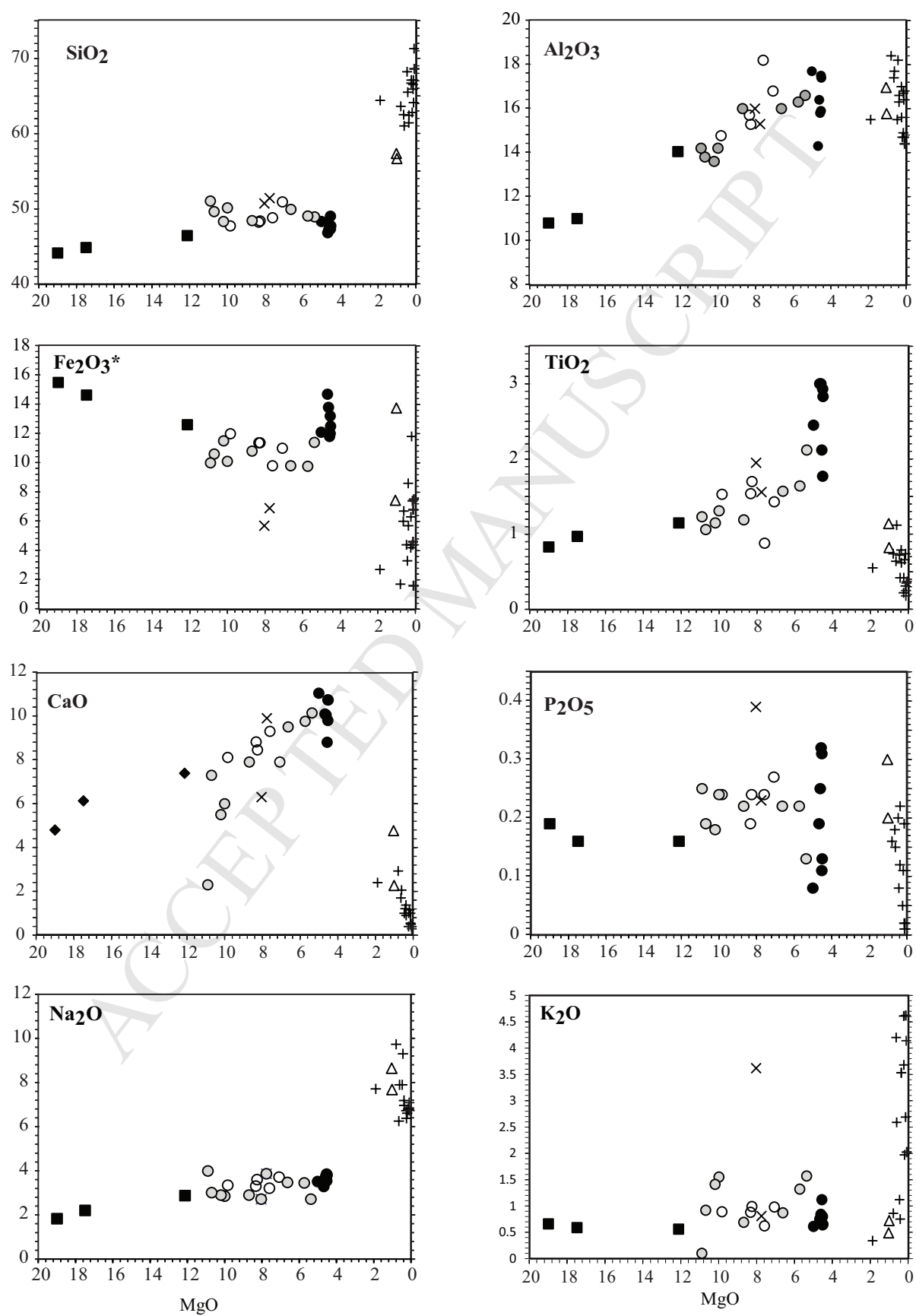
Rock type	Sample	Rb	Sr	$^{87}\text{Rb}/^{86}\text{Sr}$	$^{87}\text{Sr}/^{86}\text{Sr}$	$\pm 2\sigma$	$(^{87}\text{Sr}/^{86}\text{Sr})_i$	Sm	Nd	$^{147}\text{Sm}/^{144}\text{Nd}$	$^{143}\text{Nd}/^{144}\text{Nd}$	$\pm 2\sigma$	$\epsilon\text{Nd}_{(T)}$
Ox-Gabbro	TR8	9,87	539	0,053043	0,704715	15	0,704602	3,72	13,14	0,171892	0,512793	17	3,5
Ox-Gabbro	TR9	9,13	388	0,068143	0,703719	7	0,703574	3,67	12,21	0,182092	0,512814	5	3,7
Ox-Gabbro	TR10	6,47	574	0,032661	0,704416	22	0,704346	2,80	9,68	0,175237	0,512788	9	3,3
HA-Gabbro	TR48	33,83	436	0,224687	0,705285	19	0,704806	2,47	8,93	0,167502	0,512712	12	2,0
Monzonite	TR2	3,42	880	0,011253	0,707498	13	0,707474	6,92	27,57	0,152127	0,512678	8	1,6
Syenite	TR21	6,12	271	0,065380	0,707071	21	0,706932	9,21	41,22	0,135451	0,512722	2	2,8
Syenite	TR25	26,82	243	0,319632	0,707401	21	0,706720	8,64	36,26	0,144576	0,512799	17	4,1
Syenite	TR32	31,47	61	1,493786	0,710250	13	0,707067	9,37	36,50	0,155704	0,512789	12	3,7



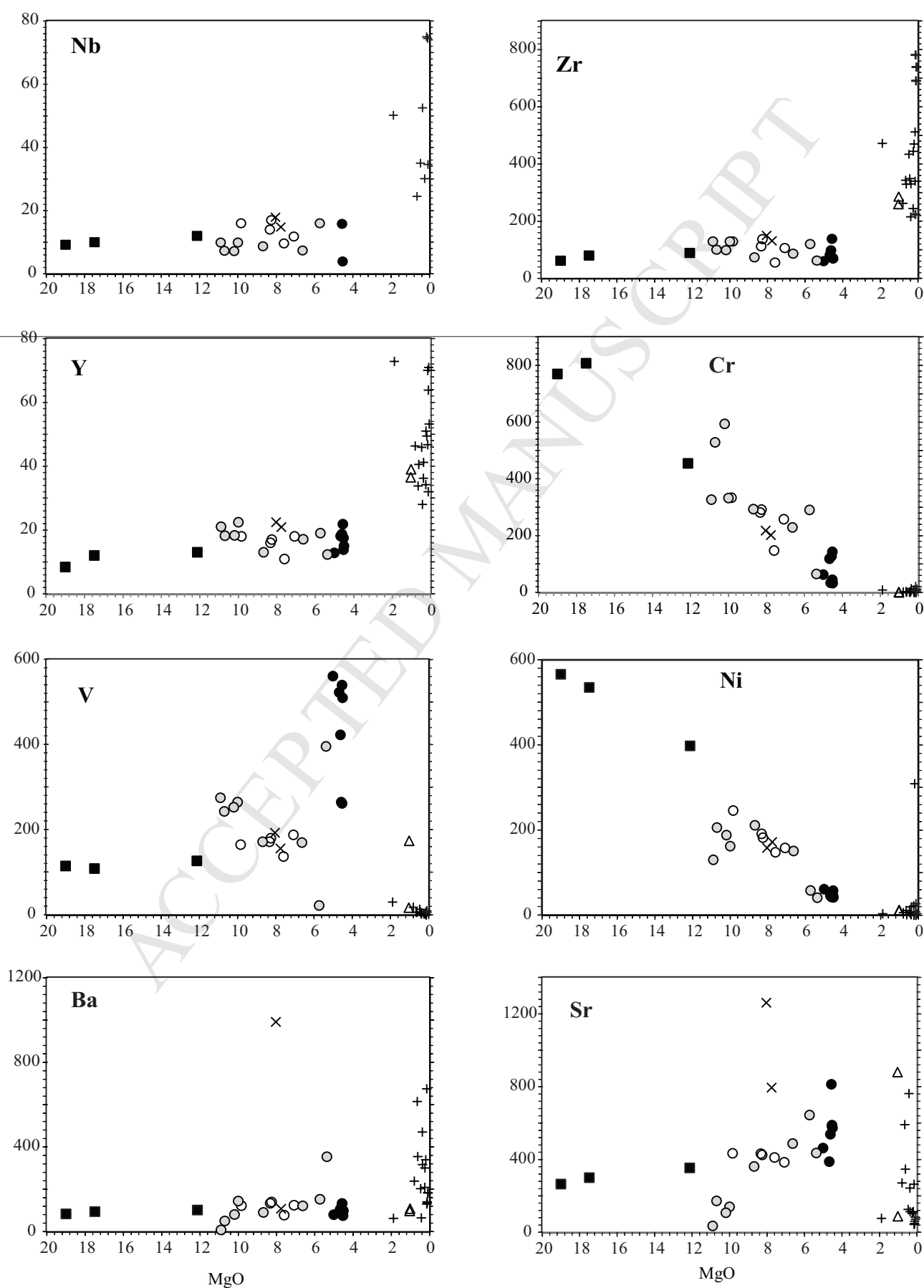


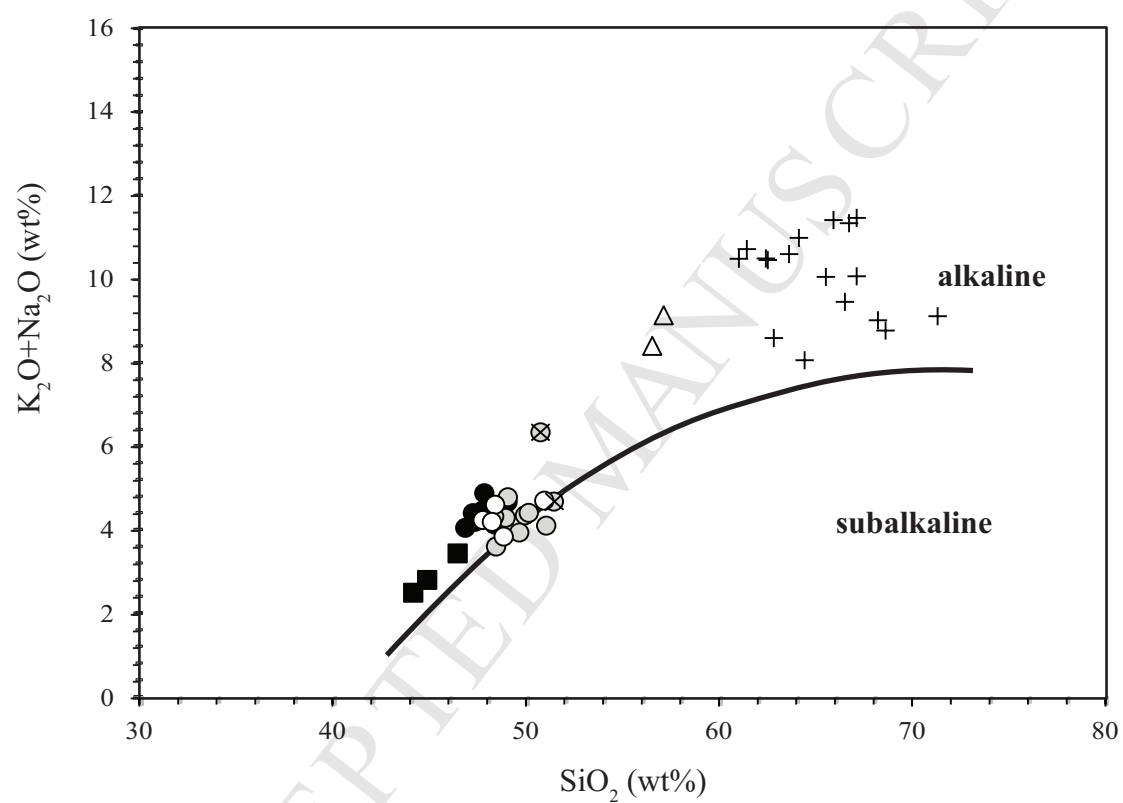


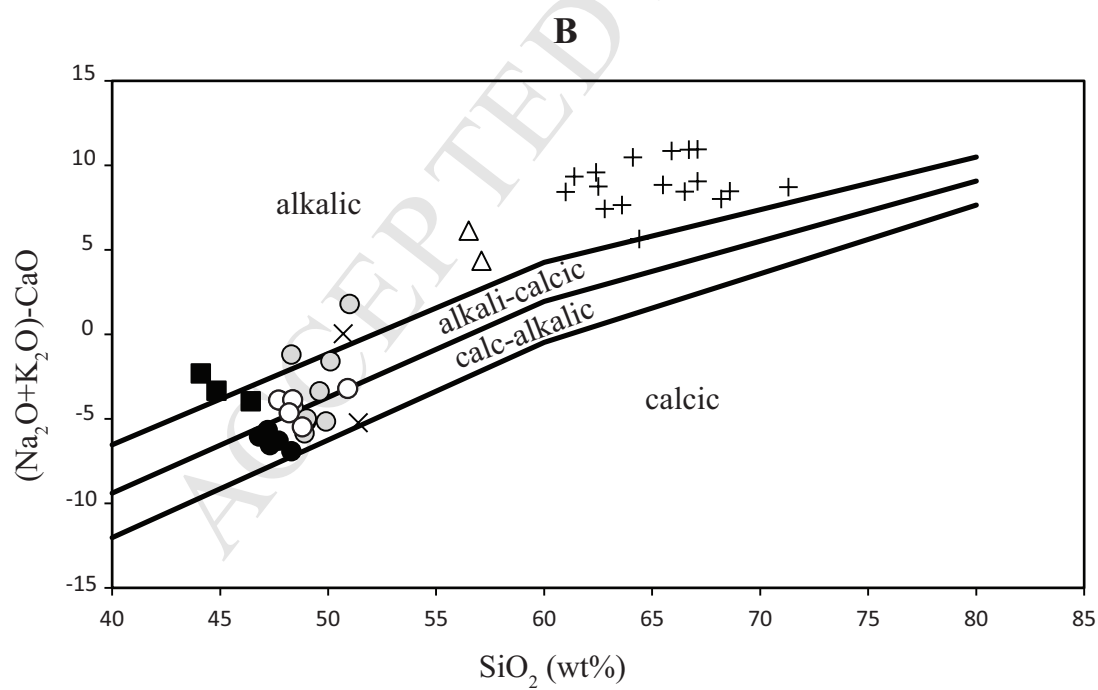
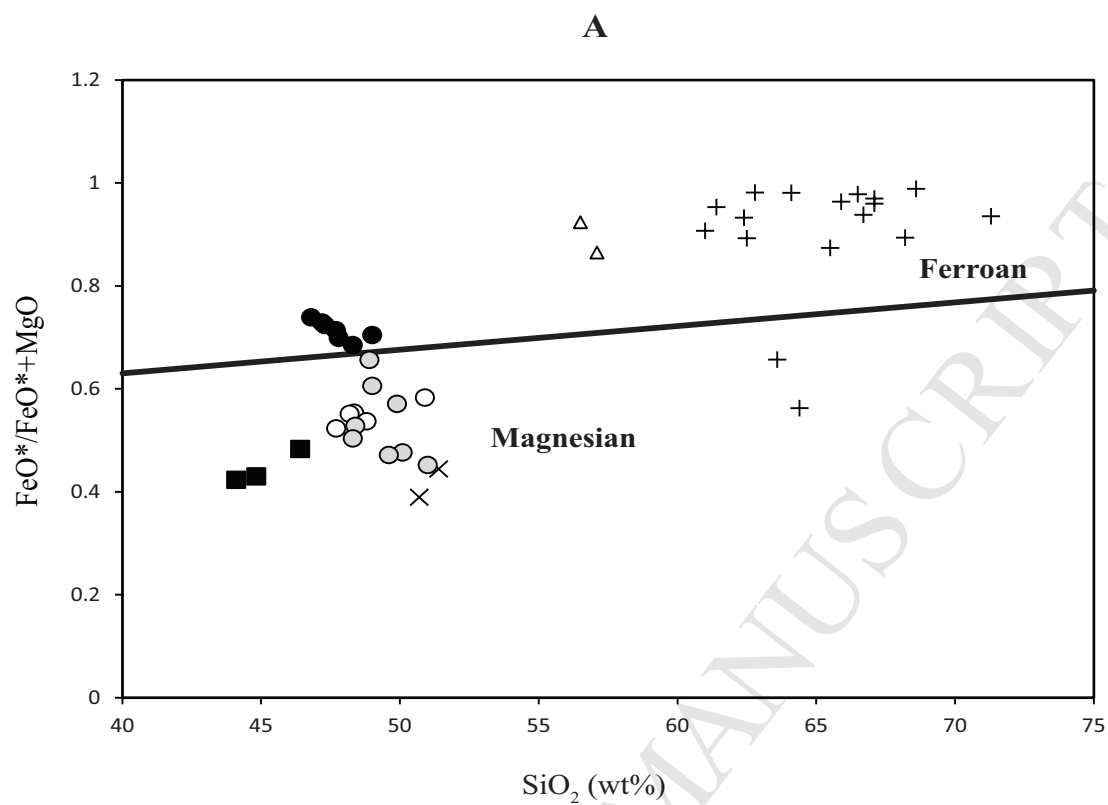
A

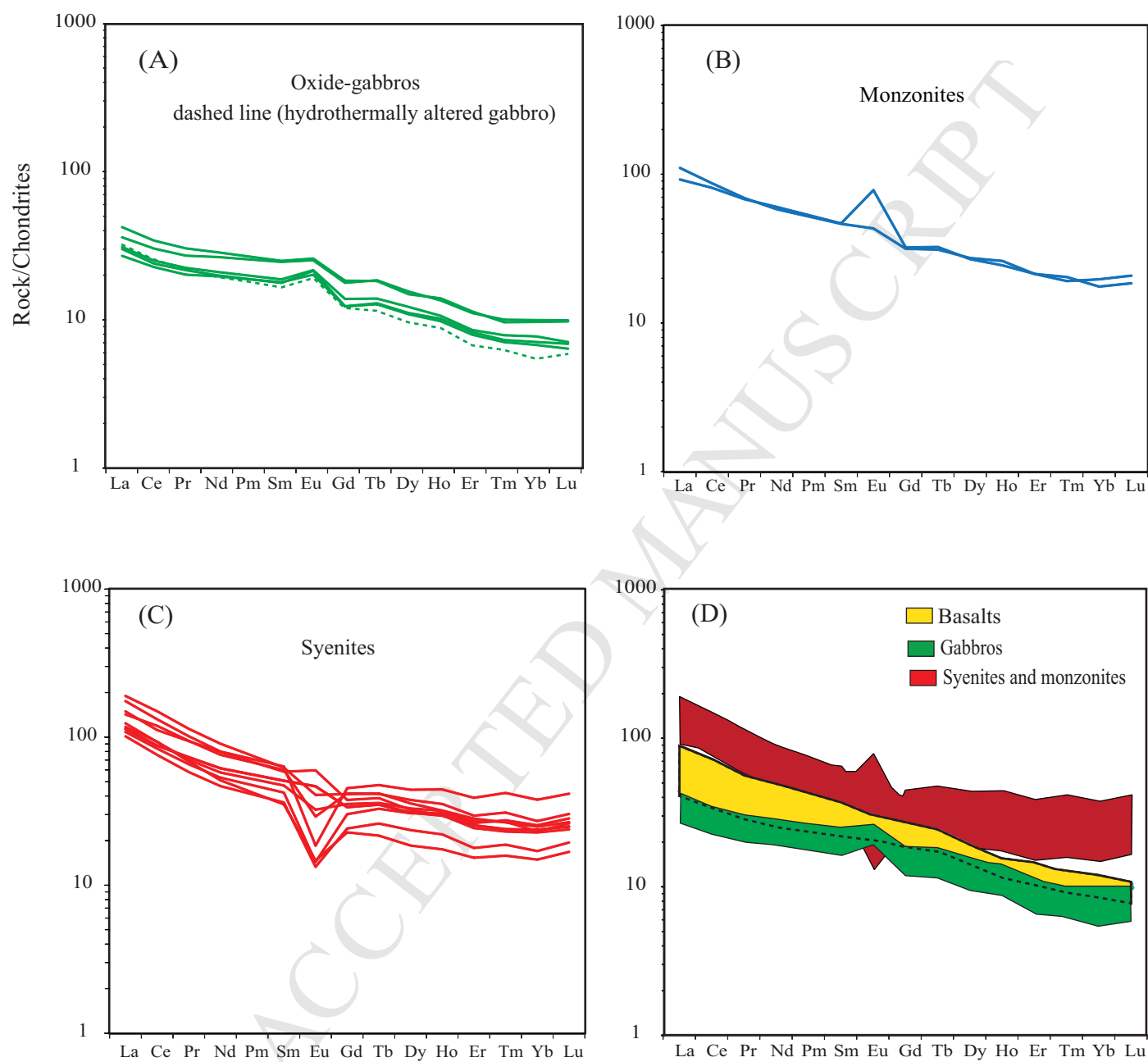


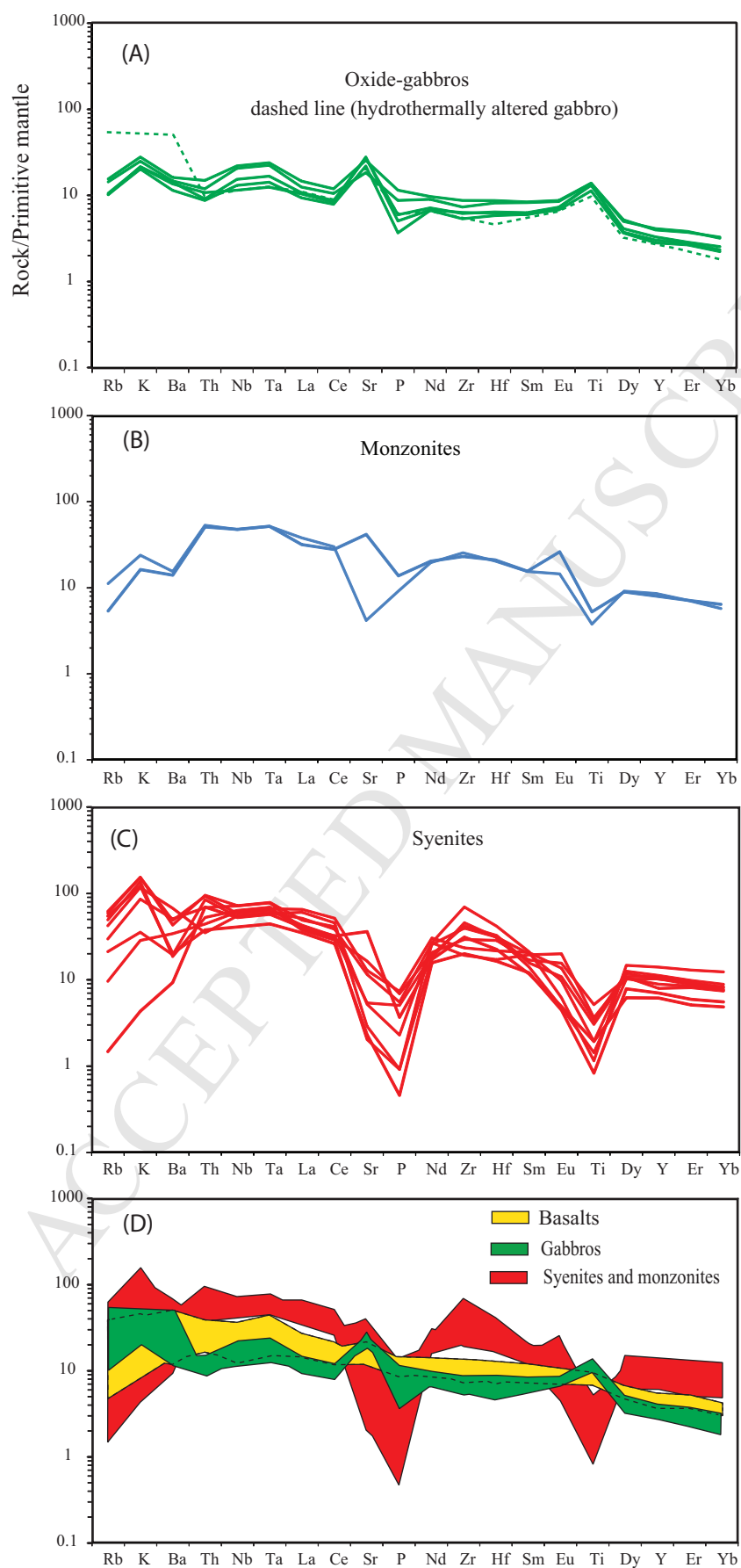
B

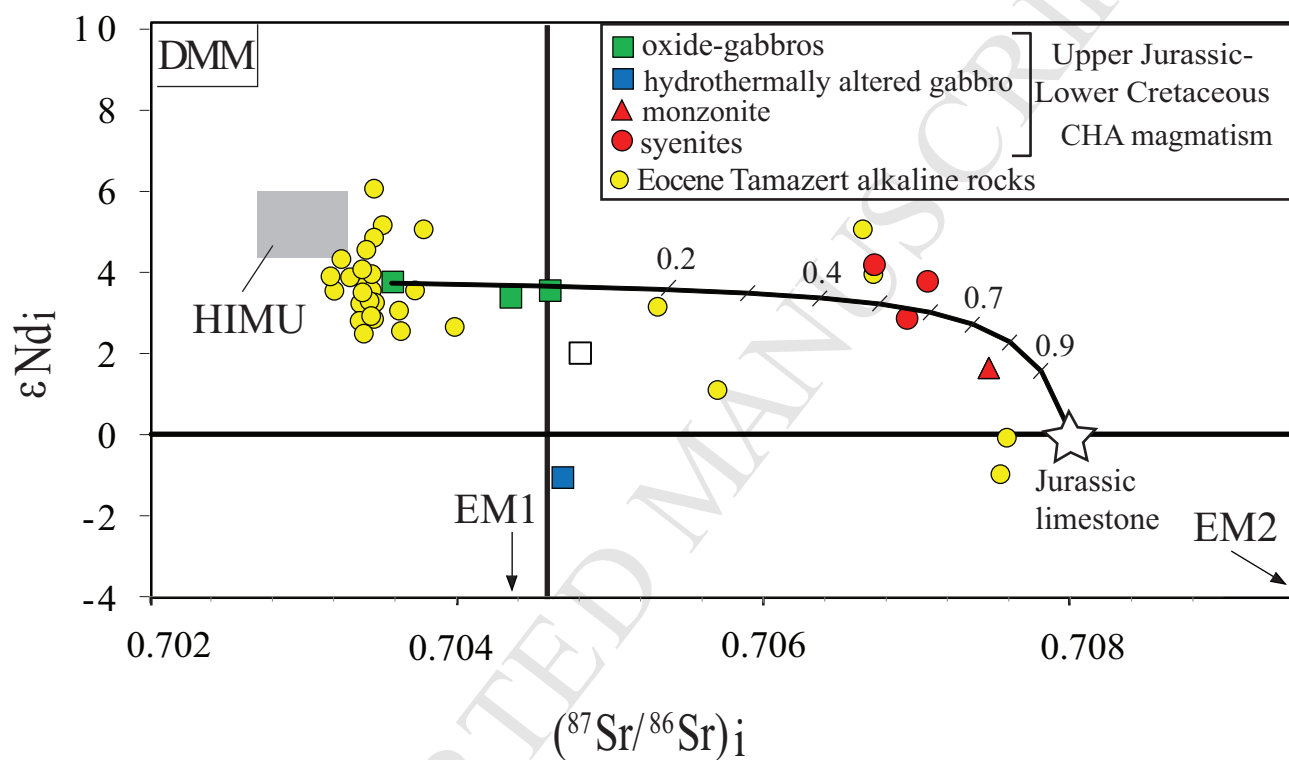


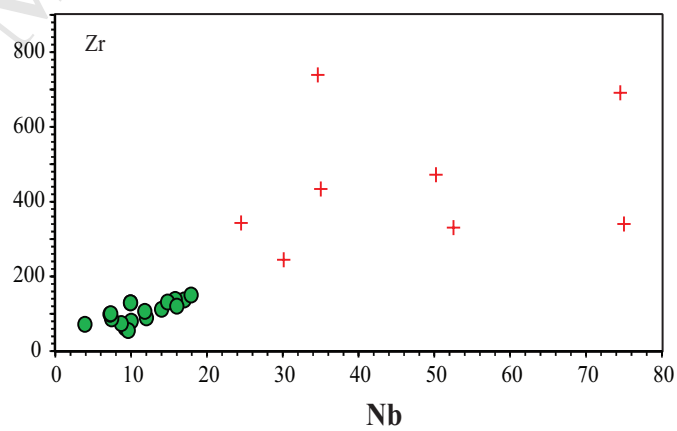
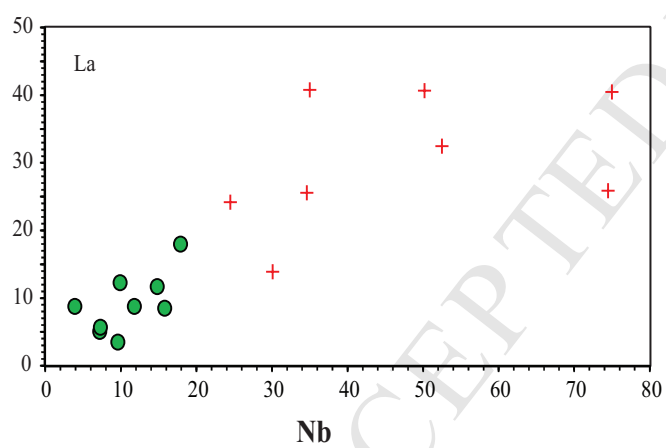
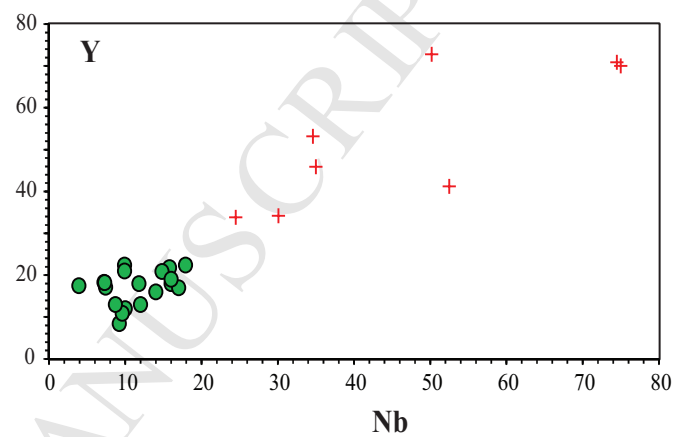
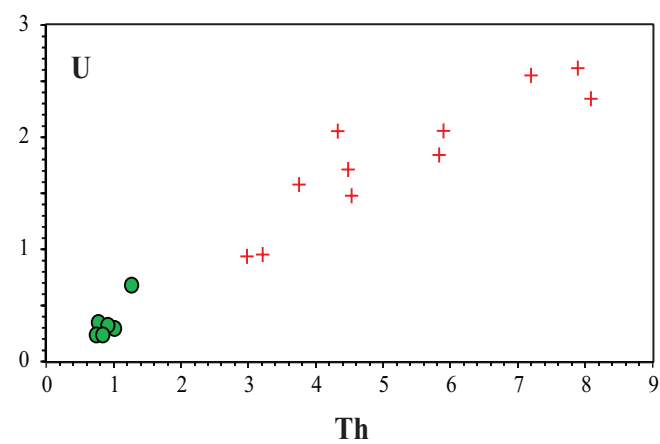


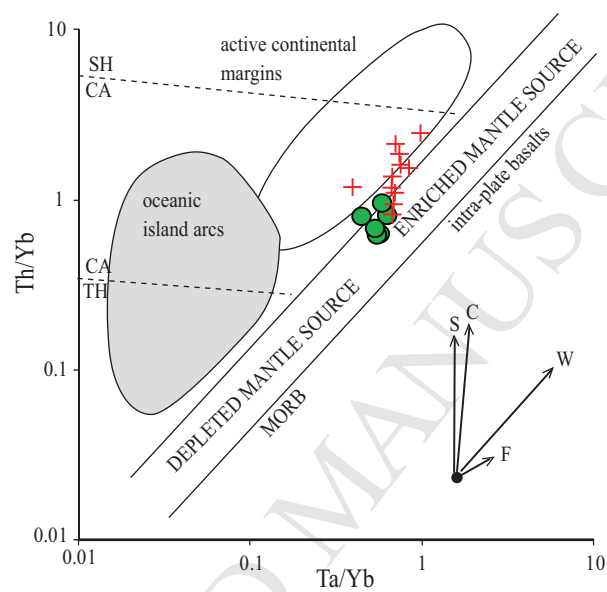


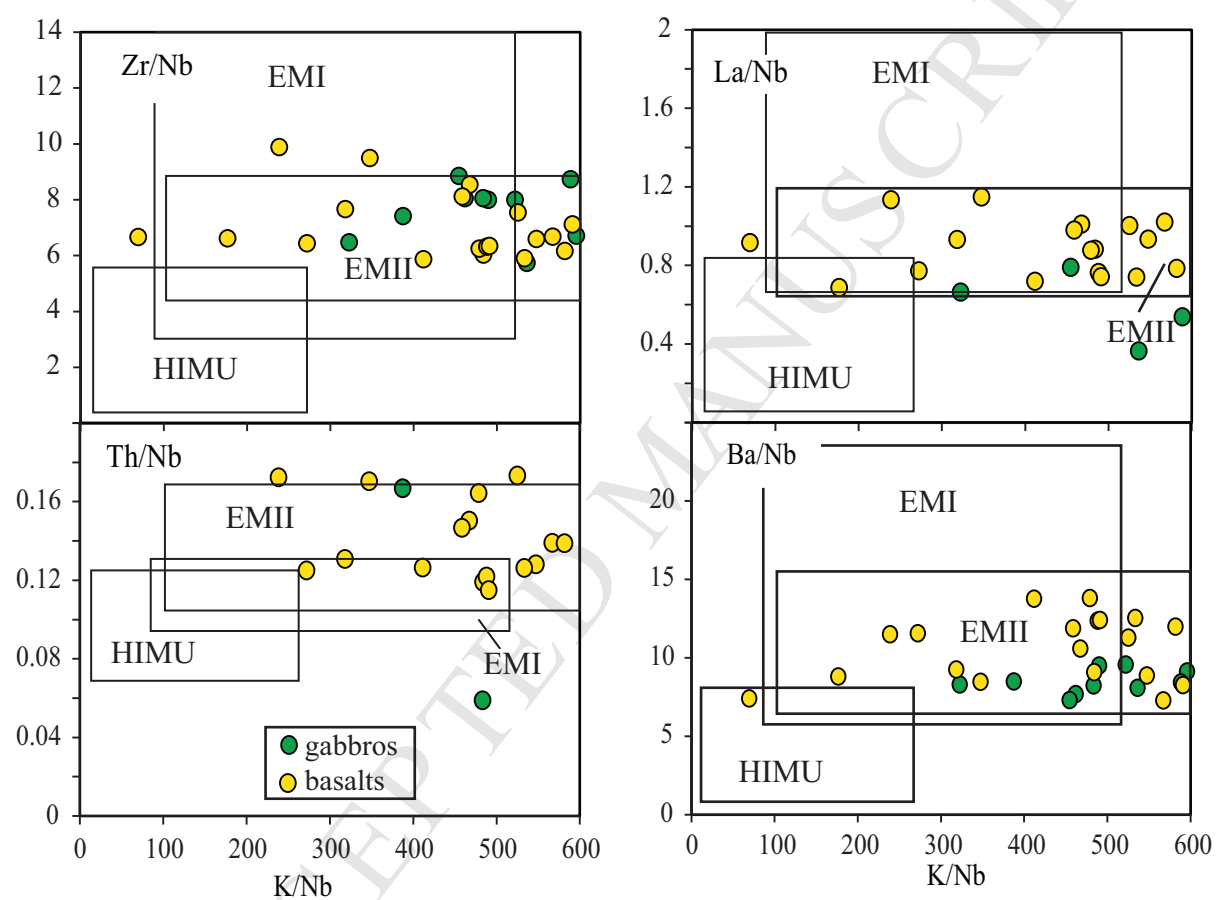


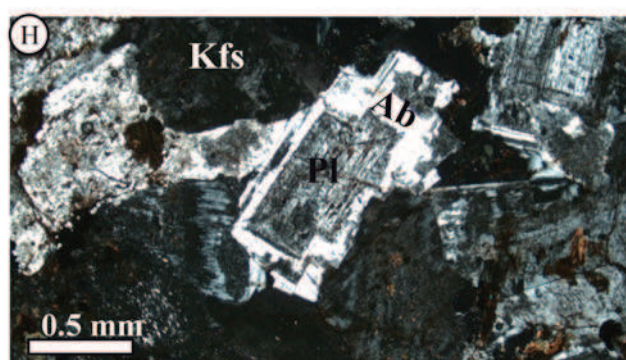
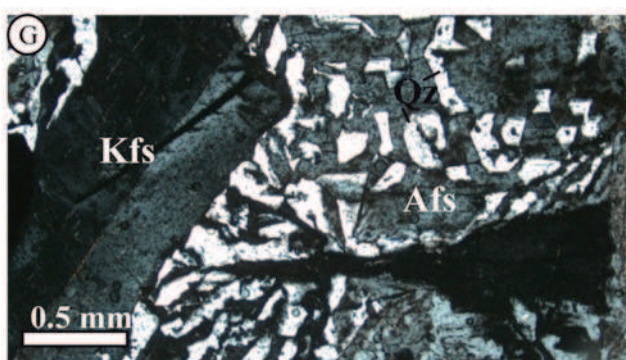
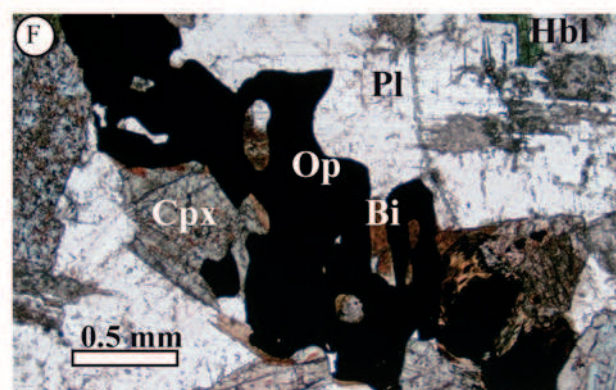
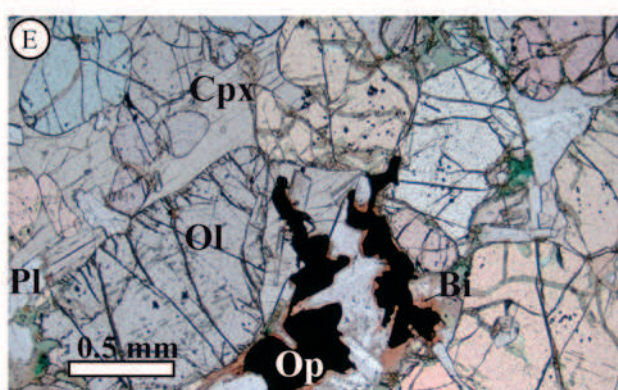
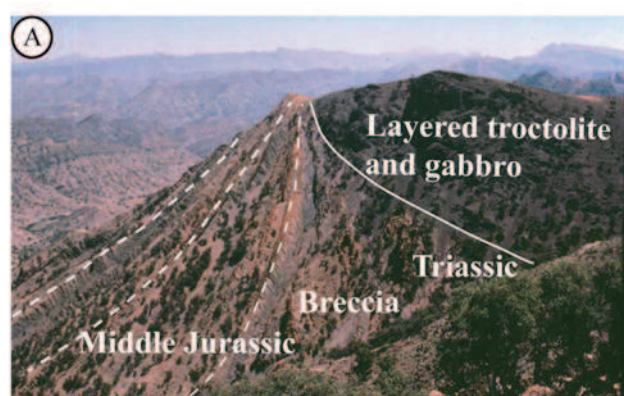












Highlights

Mesozoic transitional to moderately alkaline magmatism emplaced in the High Atlas

Fractional crystallization allowed evolution from troctolites to oxide-gabbros and syenites

Alkali metasomatism modified the Sr isotopic composition of the syenites

The Sr-Nd isotopic composition of uncontaminated gabbros indicate an enriched upper mantle

The enriched upper mantle signature is related to pre-Mesozoic geodynamic processes